



Pre-impact Thermophysical Properties and the Yarkovsky Effect of NASA DART Target (65803) Didymos

Benjamin Rozitis¹, Simon F. Green¹, Samuel L. Jackson^{1,2}, Colin Snodgrass², Cyrielle Opitom², Thomas G. Müller³, Ulrich C. Kolb¹, Steven R. Chesley⁴, R. Terik Daly⁵, Cristina A. Thomas⁶, and Andrew S. Rivkin⁵

¹ School of Physical Sciences, The Open University, Milton Keynes, UK; benjamin.rozitis@open.ac.uk

² Institute for Astronomy, University of Edinburgh, Edinburgh, UK

³ Max Planck Institute for Extraterrestrial Physics, Garching, Germany

⁴ Jet Propulsion Laboratory, Pasadena, CA, USA

⁵ The Johns Hopkins University Applied Physics Laboratory, Laurel, MD, USA

⁶ Department of Astronomy and Planetary Science, Northern Arizona University, Flagstaff, AZ, USA

Received 2023 November 6; revised 2024 January 22; accepted 2024 January 28; published 2024 March 11

Abstract

The NASA Double Asteroid Redirection Test (DART) spacecraft impacted the secondary body of the binary asteroid (65803) Didymos on 2022 September 26 and altered its orbit about the primary body. Before the DART impact, we performed visible and mid-infrared observations to constrain the pre-impact thermophysical properties of the Didymos system and to model its Yarkovsky effect. Analysis of the photometric phase curve derives a Bond albedo of 0.07 ± 0.01 , and a thermophysical analysis of the mid-infrared observations derives a thermal inertia of $320 \pm 70 \text{ J m}^{-2} \text{ K}^{-1} \text{ s}^{-1/2}$ and a thermal roughness of $40^\circ \pm 3^\circ$ rms slope. These properties are compatible with the ranges derived for other S-type near-Earth asteroids. Model-to-measurement comparisons of the Yarkovsky orbital drift for Didymos derives a bulk density of $2750 \pm 350 \text{ kg m}^{-3}$, which agrees with other independent measures based on the binary mutual orbit. This bulk density indicates that Didymos is spinning at or near its critical spin-limit at which self-gravity balances equatorial centrifugal forces. Furthermore, comparisons with the post-impact infrared observations presented in Rivkin et al. indicate no change in the thermal inertia of the Didymos system following the DART impact. Finally, orbital temperature simulations indicate that subsurface water ice is stable over geologic timescales in the polar regions if present. These findings will be investigated in more detail by the upcoming ESA Hera mission.

Unified Astronomy Thesaurus concepts: Asteroids (72); Near-Earth objects (1092); Asteroid dynamics (2210); Asteroid surfaces (2209); Infrared astronomy (786)

1. Introduction

The binary near-Earth asteroid (65803) Didymos was the target of NASA's Double Asteroid Redirection Test (DART) mission, the primary goal of which was to impact the secondary body, named Dimorphos, and alter its orbit about the primary body (Cheng et al. 2018). The DART spacecraft successfully impacted Dimorphos on 2022 September 26, 23:14 UTC and reduced the binary orbital period from 11.92 to 11.37 hr (Daly et al. 2023; Thomas et al. 2023). The resulting impact ejecta produced a momentum enhancement factor of 3.6 ± 0.2 (Cheng et al. 2023) and turned the Didymos system into an artificial active asteroid (Graykowski et al. 2023; Li et al. 2023). Before the DART impact, we performed visible and thermal-infrared observations with the Open University Physics Innovation Robotic Astronomical Telescope Explorer (OU PIRATE) and European Southern Observatory Very Large Telescope (ESO VLT) telescopes, respectively, to constrain the surface properties of the Didymos system and to predict its Yarkovsky orbital drift.

The surface response to an impacting hypervelocity projectile depends on whether the impact occurs in a gravity- or strength-dominated regime. Large asteroids lie in the gravity-dominated regime, in which the impacted material behaves as a cohesionless material, whereas in the strength-dominated regime, which

is likely to apply in the case of Dimorphos, the physical properties of the surface play a significant role in the crater formation process (Holsapple 1993).

Thermal inertia and thermal roughness are two useful properties that constrain the nature of planetary surfaces (Rozitis et al. 2020b). For instance, thermal inertia is a measure of a material's resistance to temperature change and can be used as a qualitative indicator of the regolith particle size (e.g., Gundlach & Blum 2013; Sakatani et al. 2017) and/or the porosity of rocks and boulders (e.g., Grott et al. 2019; Sakatani et al. 2021). It is defined by $\Gamma = (k\rho C_p)^{1/2}$, where k is the thermal conductivity, ρ is the density, and C_p is the heat capacity. Thermal roughness is a measure of the irregularity of a surface over spatial scales comparable to and larger than the diurnal thermal skin depth, given by $d_s = (kP/\pi\rho C_p)^{1/2}$, where P is the rotation period. It causes the thermal-infrared beaming effect where absorbed solar radiation is preferentially re-emitted back toward the Sun (e.g., Spencer 1990; Lagerros 1998; Rozitis & Green 2011). Both properties can be determined when thermal-infrared observations of a planetary body and/or surface are fitted with a suitable thermophysical model (Delbo et al. 2015 and references therein).

Thermal inertia has previously been quantified by thermophysical models for several tens of asteroids with high-quality shape models (e.g., Delbo et al. 2015; Hanuš et al. 2015, 2018a) and for hundreds more with low-quality shape models (e.g., MacLennan & Emery 2021; Hung et al. 2022). These population studies have revealed a primary trend of decreasing



Original content from this work may be used under the terms of the [Creative Commons Attribution 4.0 licence](https://creativecommons.org/licenses/by/4.0/). Any further distribution of this work must maintain attribution to the author(s) and the title of the work, journal citation and DOI.

asteroid thermal inertia with increasing size (e.g., Delbo et al. 2007, 2015; Hung et al. 2022), and a secondary trend of decreasing thermal inertia with increasing heliocentric distance (e.g., Rozitis et al. 2018; MacLennan & Emery 2021). Trends with rotation period are currently inconclusive (e.g., Harris & Drube 2016; Marciniak et al. 2019, 2021). Such trends indicate that asteroid surfaces consist predominantly of particulate regoliths where the mean particle size decreases with increasing asteroid surface gravity (Gundlach & Blum 2013; MacLennan & Emery 2022).

In an exception to these trends, the spatially resolved measurements of the C-type near-Earth asteroids (101955) Benu (Rozitis et al. 2020b, 2022) and (162173) Ryugu (Okada et al. 2020; Shimaki et al. 2020) have recently revealed that rock porosity also dictates the thermal inertia for at least these two asteroids. It has been hypothesized that such asteroids, comprising porous rocks and boulders, produce less particulate regolith from mechanical space weathering processes, such as thermal cracking and micrometeorite bombardment (Cambioni et al. 2021). Other exceptions include the very low thermal inertia surfaces determined for the rapidly rotating asteroids (29075) 1950 DA (Rozitis et al. 2014) and 2016 GE1 (Fenucci et al. 2023). These two cases indicate the possible presence of inter-particle cohesive forces that prevent centrifugal mass loss and structural breakup (e.g., Sánchez & Scheeres 2020).

Binary asteroids comprise $\sim 15\%$ of the near-Earth population (Pravec et al. 2006), but only three have had their thermal inertia determined directly by a thermophysical model. These determinations include $140^{+140}_{-100} \text{ J m}^{-2} \text{ K}^{-1} \text{ s}^{-1/2}$ for (1862) Apollo (Rozitis et al. 2013), 120 ± 50 (Wolters et al. 2011) and 80 ± 40 (Yu et al. 2014) $\text{J m}^{-2} \text{ K}^{-1} \text{ s}^{-1/2}$ for (175706) 1996 FG3, and $170 \pm 30 \text{ J m}^{-2} \text{ K}^{-1} \text{ s}^{-1/2}$ for (276049) 2002 CE26 (Rozitis et al. 2018). These moderately low values indicate that their surfaces are composed of millimeter- to centimeter-sized particles (Gundlach & Blum 2013) and/or of highly porous rocks and boulders (Rozitis et al. 2020b). In contrast, Delbo et al. (2011) estimated the average thermal inertia of eight binary near-Earth asteroids to be $480 \pm 70 \text{ J m}^{-2} \text{ K}^{-1} \text{ s}^{-1/2}$ by comparing their distribution of measured beaming parameters with theoretical predictions made by a thermophysical model. This contrasted with an average value of $200 \pm 40 \text{ J m}^{-2} \text{ K}^{-1} \text{ s}^{-1/2}$ determined in a previous study for solitary near-Earth asteroids (Delbo et al. 2007), and they conclude that their sample of eight binary near-Earth asteroids must be relatively devoid of fine-grained regolith. In comparison to other asteroid populations, Marchis et al. (2012) determined the thermal inertia of seven main-belt binary asteroids to be $\leq 100 \text{ J m}^{-2} \text{ K}^{-1} \text{ s}^{-1/2}$, and Mueller et al. (2010) determined the thermal inertia of the eclipsing binary Trojan asteroid (617) Patroclus–Menoetius to be $20 \pm 15 \text{ J m}^{-2} \text{ K}^{-1} \text{ s}^{-1/2}$. However, these thermal inertia values did not differ significantly from other solitary asteroids in the same population class (e.g., Delbo & Tanga 2009).

Thermal roughness is generally difficult to constrain because of a strong degeneracy with thermal inertia (Müller et al. 2012; Rozitis 2017), and requires observations acquired at multiple wavelengths and phase angles for accurate determination (Rozitis & Green 2011; Davidsson et al. 2015). For the few successful cases, asteroid thermal roughness (i.e., $\sim 30^\circ$ – 50° rms slope; Spencer 1990; Rozitis 2017; Rozitis et al. 2020b; Shimaki et al. 2020) is generally higher than that of the Moon (i.e., $\sim 20^\circ$ – 35° rms slope; Rozitis & Green 2011; Bandfield

et al. 2015; Müller et al. 2021), but it is unclear whether any general trends exist within the asteroid population due to the limited number of constraints. However, for asteroid Benu, spatially resolved measurements show that thermal roughness arises from the shape and number density of rocks and boulders not resolved by the topography included in the thermophysical model (i.e., topography at $< 6 \text{ m}$ spatial scales; Rozitis et al. 2020b), and it correlates with geologic units (Jawin et al. 2022) and other photometric and physical measures of surface roughness (Daly et al. 2020; Golish et al. 2021; Li et al. 2021). At present, thermal roughness has not been tightly constrained for any binary asteroid.

Thermal inertia and thermal roughness, in addition to being useful diagnostic measures of planetary surfaces, also dictate the orbital and spin evolutions of small ($< 10 \text{ km}$) asteroids through the Yarkovsky and YORP (Yarkovsky–O’Keefe–Radzievskii–Paddack) effects, respectively (Vokrouhlický et al. 2015). For instance, thermal inertia leads to a net-photon-recoil force exerted on the asteroid afternoon side via the delayed thermal re-emission of absorbed sunlight, which causes the asteroid orbit to expand or shrink depending on whether the asteroid is a prograde or retrograde rotator, respectively. Thermal roughness enhances the effectiveness of the Yarkovsky recoil force by directing more of the thermally emitted photons into the orbital plane of the asteroid (Rozitis & Green 2012). Similarly, the asymmetric reflection and thermal re-emission of incident sunlight from an irregularly shaped and/or surfaced asteroid can lead to net torques that cause an asteroid to spin up or spin down with time and shift its spin-axis orientation. The rates at which these components of YORP happen depend critically on the asteroid’s thermal inertia and thermal roughness. Both effects are likely to have played large roles in the formation and evolution of small binary asteroids via centrifugal mass loss from YORP spin-up (e.g., Walsh et al. 2008), and orbital perturbation from the main belt by the Yarkovsky effect (e.g., Bottke et al. 2006).

Thermophysical models are useful tools for evaluating thermal inertia, thermal roughness, and the Yarkovsky and YORP effects (Delbo et al. 2015; Vokrouhlický et al. 2015), but they require several predefined inputs to make useful and accurate predictions. These include the asteroid shape/topography, pole orientation, rotation period, bolometric and spectral emissivity, and the Bond albedo. As summarized in Müller et al. (2018), the shape and spin state can be derived from light-curve and/or radar inversion (Hudson 1994; Kaasalainen & Torppa 2001), adaptive optics and stellar occultation events (Hanuš et al. 2017), stereophotoclinometry from direct spacecraft imaging (Gaskell et al. 2008), and via spacecraft laser ranging (Daly et al. 2020). Assumptions are typically made about the bolometric and spectral emissivity based on the asteroid’s taxonomic class. Finally, the Bond albedo is typically derived from the asteroid absolute magnitude H and phase parameter G in combination with the asteroid diameter (Bowell et al. 1989; Fowler & Chillemi 1992). However, such quantities are susceptible to catalog biases (Pravec et al. 2012) and aspect effects (Jackson et al. 2022), and therefore well-constructed phase curves are required to derive an accurate value for the Bond albedo. Furthermore, phase curves can also provide additional diagnostic information on the composition of the asteroid surface (Oszkiewicz et al. 2012; Penttilä et al. 2016).

Table 1
Observational Circumstances and Photometry of the Didymos System with OU PIRATE

Observation Date	Heliocentric Distance (au)	Geocentric Distance (au)	Phase Angle (°)	Reduced V -magnitude
2022 Jul 29	1.312	0.334	23.7	19.29 ± 0.07
2022 Jul 30	1.307	0.327	23.4	19.28 ± 0.06
2022 Jul 31	1.301	0.320	23.2	19.28 ± 0.07
2022 Aug 3	1.285	0.299	22.4	19.24 ± 0.06
2022 Aug 4	1.280	0.293	22.2	19.25 ± 0.06
2022 Aug 5	1.274	0.286	21.9	19.25 ± 0.07

The DART encounter at the Didymos system provided the first close-up view of a binary near-Earth asteroid, in addition to being the first direct test of the kinetic impactor deflection technique (Cheng et al. 2018). Furthermore, the ESA Hera mission will arrive at the Didymos system in late 2026 to perform additional studies of the physical properties of Didymos and Dimorphos, the crater made by the DART impact, and the momentum enhancement factor (Michel et al. 2022). Therefore, determination of the thermal inertia and thermal roughness for the Didymos system would provide complementary insights into the surface morphology of the impact site, the nature and formation of binary asteroids, and how the Yarkovsky effect operates on such planetary bodies. In the subsequent sections of this work, we constrain the Bond albedo through photometric observations and phase-curve modeling, we determine the thermal inertia and thermal roughness from mid-infrared observations and thermophysical modeling, and we compute the Yarkovsky orbital drift for the Didymos system. The implications of our results are then discussed considering the DART mission findings, and temperature predictions are made for the future rendezvous by the ESA Hera mission.

2. Observations and Data Reduction

2.1. Photometric Observations

The phase curve of Didymos was previously derived by Kitazato et al. (2004), but in the R band from just four photometric measurements. They derived $H_R = 17.70 \pm 0.03$ and $G_R = 0.20 \pm 0.02$, and they applied a $V - R = 0.46 \pm 0.01$ color term to estimate $H_V = 18.16 \pm 0.04$. In this study, we sought to confirm and refine the H_V and G_V values because our subsequent thermophysical modeling requires the Bond albedo to be derived in the V band. To supplement the Kitazato et al. (2004) photometry, we collected additional V -band photometric measurements of Didymos before the DART impact with the OU PIRATE telescope (Kolb et al. 2018; Jackson et al. 2021).

Observations of the Didymos system were collected from 2022 July 29 until 2022 August 5 in the Johnson V and R bands using 300 s exposures (see Table 1). Photometry of Didymos was extracted using a custom asteroid data processing pipeline for PIRATE, making use of the SExtractor software package (Bertin & Arnouts 1996) for the raw photometry, and astrometry.net (Lang et al. 2010) for plate-solving the images. The instrumental color derived from the multiband observations was used to ensure adequate color-correction when calibrating the instrumental magnitudes into the Pan-STARRS r_{P1} band (Tonry et al. 2012). The PIRATE light curves were then converted into the Johnson V band using transformation

equations from Tonry et al. (2012). Full details of the PIRATE data reduction and calibration procedures can be found in Jackson et al. (2021).

To produce the data for the phase curve, the individual light curves were simply averaged over a night of observations, and the uncertainty is reported as the standard deviation of the data added in quadrature with the calibration uncertainty of the entire light curve. Rotation period averaging was not necessary, as Didymos did not show rotation brightness variations greater than the calibration uncertainty in our observations. Therefore, any offsets introduced in the phase curve will be small compared to the measurement uncertainties and will average out over observations taken over different nights.

For producing the combined phase curve data set, the R -band data of Kitazato et al. (2004) were converted to the V band using their derived $V - R$ color. Here, we assumed that there were no significant differences in the phase curve slopes between the V and R bands beyond the uncertainties of the measurements. Any differences between the slopes due to phase reddening would be small at the range of phase angles covered by these data. The combined phase curve data set was then analyzed using the H , G photometric system (Bowell et al. 1989), as described further in Section 3.1.

Finally, for an independent comparison with data acquired over multiple illumination and observation geometries, we downloaded all photometric measurements reported in the V band to the Minor Planet Center (MPC) prior to the DART impact (i.e., 267 observations in total). Photometric measurements reported to the MPC are typically very noisy because of different telescopes, observational circumstances (e.g., random sampling of asteroid light curves), and data reduction techniques being used. However, such systematics and noise tend to average out when many observations (i.e., hundreds) are acquired over long periods of time (Williams 2013). We did not retrieve photometric measurements reported in other imaging bands (e.g., R band), because the raw imaging data were not available to compute the appropriate color corrections for conversion into the V band.

2.2. Thermal-infrared Observations

To constrain the thermal inertia and thermal roughness of the Didymos system, we acquired mid-infrared imaging and spectroscopy with the VISIR instrument (Lagage et al. 2004) on Unit 2 “Kueyen” of the 8.2 m VLT array at ESO’s Paranal Observatory in Chile. In particular, Didymos was observed on 2022 August 24 in imaging mode, and again on 2022 September 26 (i.e., the night before DART impact) in both imaging and spectroscopy modes (see Table 2 for the observational circumstances).

In imaging mode, VISIR had a pixel scale of $0''.045 \text{ pixel}^{-1}$ and a total field of view of $38''$ by $38''$, and our observations were chop-nodded with perpendicular throws of $8''$ for sky-background subtraction. We utilized the M band ($4.74 \mu\text{m}$), J8.9 ($8.7 \mu\text{m}$), B12.4 ($12.4 \mu\text{m}$), and Q1 ($17.75 \mu\text{m}$) filters to measure the spectral shape of the thermal emission from the Didymos system, and these filters were alternately sequenced with the B10.7 ($10.62 \mu\text{m}$) filter to measure the temporal flux variation. Integration times were chosen to give a minimum signal-to-noise ratio (S/N) of 100 in each filter (except the M band), and standard stars of similar airmass to Didymos and within 2 hr of R.A. were observed for calibration purposes. At this high S/N, the absolute calibration was sensitive to temporal variations in the atmospheric seeing conditions, and

Table 2
Observational Circumstances of the Didymos System with ESO VLT VISIR

Observation Date	Heliocentric Distance (au)	Heliocentric Longitude (°)	Heliocentric Latitude (°)	Geocentric Distance (au)	Geocentric Longitude (°)	Geocentric Latitude (°)	Phase Angle (°)
2022 Aug 24	1.176	332.6	−3.3	0.180	343.7	−22.5	21.8
2022 Sep 26	1.048	4.2	−3.2	0.077	32.9	−49.4	52.2

thus we conducted repeated measurements of the standard stars to quantify the atmospheric calibration uncertainty in each filter. In total, we acquired 2.3 and 3.1 hr of observations on the two nights, which each approximately covered one rotation of the Didymos primary body (i.e., 2.26 hr). Conditions were photometric on both nights with subarcsecond seeing and precipitable water vapor levels of <2 mm.

Following the observations, the raw imaging data from each night were downloaded and then reduced using the ESO Gasgano pipeline software.⁷ For each reduced image, the FWHM of the Didymos or standard star point source was measured, and aperture photometry was subsequently performed using an aperture radius of 1.7 times the FWHM (Collins et al. 2017). The source counts were then converted to physical flux units by using the conversion factors derived from the standard star observations and their catalog flux values⁸ (Table A1; derived from Cohen et al. 1999), and the effective wavelengths and color corrections for each filter were determined from the filter response functions.⁹ The total flux uncertainties were calculated by combining in quadrature the uncertainties resulting from the target S/N, atmospheric seeing variability, and the precision of the standard star flux catalog. Here, the resulting total flux uncertainties ranged from ~4% for the B10.7 filter to ~11% for the *M*-band filter. The derived fluxes (Table A2) were checked for consistency by performing a parallel data reduction using the alternative ESO Reflex pipeline software (Freudling et al. 2013), which produced values that were identical to the Gasgano derived values within their respective uncertainties.

In spectroscopy mode, we used the low-resolution setting with a slit width of 1", which provided a resolving power of ~300 in the 8–13 μm wavelength range. Again, our integration times were chosen to give a minimum S/N of 100 at ~10 μm , and the observations were parallel chop-nodded with a throw of 10" for sky-background subtraction. For calibration, we observed one of our standard stars twice, i.e., HD26967 just before and after the Didymos observations.

Similarly, after the observations, the raw spectroscopy data were downloaded and reduced using the ESO Gasgano pipeline software. Here, Gasgano automatically applied optimally sized apertures to extract the spectral data with the highest possible S/N, and so no manual intervention was necessary. The data calibration was performed separately for each of the two standard star observations, and the resulting two extractions of the Didymos data were averaged. Subsequently, we binned the spectral data into 0.1 μm wide wavelength bins to reduce noise in the extracted Didymos spectrum, and we scaled the absolute flux by a factor of 1.84 ± 0.04 so that it lined up with the flux levels derived from the photometry. This flux scaling was necessary because Gasgano used different sized apertures for Didymos and the standard star. After flux scaling, the Didymos

spectrum confirmed the spectral shape derived from the photometry. As with imaging, the extracted spectrum (Table A3) was checked for consistency by performing a parallel data reduction using the alternative ESO Reflex pipeline software, which gave identical results.

3. Photometric Phase Curve

3.1. Phase-curve Modeling

For use in the subsequent thermophysical modeling, we estimated the Bond albedo of the Didymos system by fitting the photometric data (i.e., the reduced *V*-band magnitudes $V(\alpha)$) with the two-parameter *H*, *G* model defined by

$$V(\alpha) = H - 2.5 \log_{10}[(1 - G)\Phi_1(\alpha) + G\Phi_2(\alpha)], \quad (1)$$

where *H* is the absolute magnitude, *G* is the phase parameter, and $\Phi_1(\alpha)$ and $\Phi_2(\alpha)$ are functions that describe the phase-curve behavior with phase angle α (Bowell et al. 1989). From the derived absolute magnitude, the geometric albedo of the Didymos system, p_V , can be calculated using

$$p_V = \left(\frac{10^{-\frac{H}{5}} 1329}{D_{\text{EFF}}} \right)^2, \quad (2)$$

where D_{EFF} is the combined cross-sectional diameter of Didymos and Dimorphos (Fowler & Chillemi 1992). Finally, the Bond albedo, A_B , can be determined from the geometric albedo and phase parameter using

$$A_B = (0.290 + 0.684G)p_V. \quad (3)$$

As demonstrated in Jackson et al. (2022), aspect effects can also influence the observed phase-curve behavior and affect the derived *H* and *G* values. To investigate any potential systematics in the Didymos phase curves, we implemented a shape-based Hapke model (Hapke 2012; Jackson et al. 2022) utilizing the shape models of Didymos and Dimorphos derived from DART images taken prior to impact (Barnouin et al. 2023; Daly et al. 2024). In this model, the bidirectional reflectance, r_{BI} , of each facet is calculated using

$$r_{\text{BI}} = \frac{\omega}{4\pi} \frac{\mu_i}{\mu_i + \mu_e} [(1 + B(\alpha, B_0, h))p(\alpha, g) - 1 + H(\mu_i, \omega)H(\mu_e, \omega)]S(i, e, \psi, \theta), \quad (4)$$

where ω is the single-scattering albedo, and μ_i and μ_e are the effective cosines of the angles of incidence *i* and emission *e* after accounting for macroscopic surface roughness, respectively. Additionally, $B(\alpha, B_0, h)$, $H(\mu, \omega)$, $p(\alpha, g)$, and $S(i, e, \psi, \theta)$ are functions that evaluate the opposition effect, multiple scattering, the single-particle phase function, and shadowing, respectively. Here, B_0 is the opposition effect amplitude, *h* is the opposition effect width, *g* is the asymmetry of the single-particle function, and θ is the macroscopic surface roughness.

⁷ <https://www.eso.org/sci/software/gasgano.html>

⁸ <https://www.eso.org/sci/facilities/paranal/instruments/visir/tools.html>

⁹ <https://www.eso.org/sci/facilities/paranal/instruments/visir/inst.html>

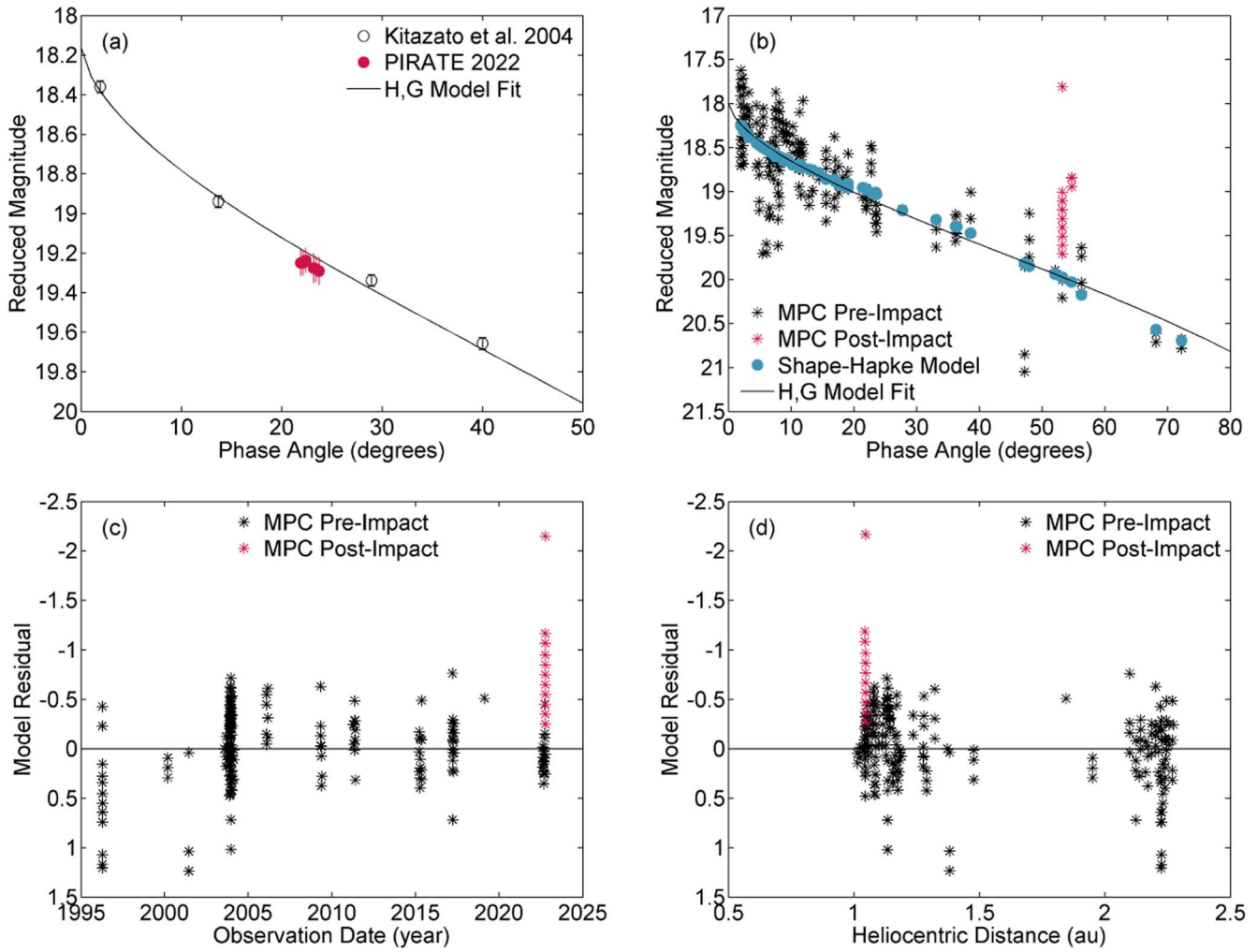


Figure 1. Photometric phase curve and modeling of the Didymos system. (a) Observations acquired by the PIRATE telescope in 2022 combined with historical observations reported in Kitazato et al. (2004). The combined data set has been fit with the two-parameter H, G model. (b) Observations reported to the Minor Planet Center (MPC) in the V band. This data set has been fit with both a shape-based Hapke model and the two-parameter H, G model. (c) Residuals of the shape-based Hapke model as a function of observation date. (d) Same as panel (c) but as a function of heliocentric distance. In panels (b)–(d), the MPC observations reported immediately post-impact are highlighted (red asterisks) to demonstrate the DART-induced increase in brightness of the Didymos system.

The reflected flux from facet j reaching the observer, $F_{\text{REF}, j}$, is then calculated as

$$F_{\text{REF}, j} = \frac{F_{\text{SUN}, \lambda} r_{\text{BI}} A_j \cos(e)}{r^2 \Delta^2}, \quad (5)$$

where $F_{\text{SUN}, \lambda}$ is the incident spectral solar flux at 1 au (i.e., $1.896 \text{ W m}^{-2} \text{ nm}^{-1}$ at 545 nm; Gueymard 2004), A_j is the area of the facet, and r and Δ are the heliocentric and geocentric distances of the asteroid, respectively. Finally, the facet flux is summed across all illuminated and visible facets, and converted to a reduced V -band magnitude using

$$V(\alpha) = -2.5 \log_{10} \left(\frac{\sum_j F_{\text{REF}, j}}{V_0} \right) - 5 \log_{10}(r \Delta), \quad (6)$$

where V_0 is the zero-point flux in the Johnson V band (i.e., $3.631 \times 10^{-11} \text{ W m}^{-2} \text{ nm}^{-1}$; Bessell et al. 1998). For a predefined set of Hapke parameters, the shape-based Hapke model was run for specified photometric measurements utilizing the geometrical calculations implemented in the Advanced Thermophysical Model (ATPM; Rozitis & Green

2011, 2012, 2013) with the asteroid ephemeris retrieved from the JPL Horizons System.¹⁰

3.2. Analysis and Results

Figure 1(a) demonstrates the H, G model fit to the Kitazato et al. (2004) and PIRATE V -band data after performing chi-square minimization. In this fit, the derived H_V and G_V parameters were 18.16 ± 0.06 and 0.18 ± 0.04 , respectively, which are consistent with the values determined previously by Kitazato et al. (2004). This absolute magnitude gives a geometric albedo of 0.17 ± 0.01 , as calculated from Equation (2) when utilizing the combined cross-sectional diameter of 0.745 ± 0.017 km for Didymos and Dimorphos (i.e., calculated from the diameters of 0.730 ± 0.017 and 0.150 ± 0.003 km for Didymos and Dimorphos, respectively; Barnouin et al. 2023; Daly et al. 2024). Finally, the phase parameter gives a Bond albedo of 0.07 ± 0.01 , as calculated from Equation (3), which is compatible with the range of 0.07–0.12 determined previously for other S-type asteroids (Domingue et al. 2002).

¹⁰ <https://ssd.jpl.nasa.gov/horizons/>

Similarly, Figure 1(b) demonstrates the H, G model fit to the MPC data after performing least-squares minimization with a Monte Carlo bootstrap method to estimate the fit uncertainties. In this case, the derived H_V and G_V parameters were 18.00 ± 0.05 and 0.14 ± 0.04 , which are partially consistent with the results obtained from the combined fit of the Kitazato et al. (2004) and PIRATE data. Here, the absolute magnitudes differ by $\sim 2\sigma$, which could be explained by a catalog bias (e.g., Pravec et al. 2012). Nevertheless, these phase-curve parameters result in geometric and Bond albedos of 0.20 ± 0.01 and 0.08 ± 0.01 , respectively, as calculated from Equations (2) and (3).

To investigate potential aspect effects, we ran the shape-based Hapke model for the observational circumstances of the MPC data assuming average S-type Hapke parameters (i.e., $\omega = 0.23$, $B_0 = 1.32$, $h = 0.02$, $g = -0.35$, and $\theta = 20^\circ$; Helfenstein & Veverka 1989), and afterwards applied a systematic offset of -0.06 mag to the model predictions to ensure that the average model magnitude was identical to the average magnitude of the data. This offset accounted for a small possible difference in the single-scattering albedo between that assumed in the model and the actual value of the Didymos system. Figure 1(b) also shows the predictions of the shape-based Hapke model, and it demonstrates that aspect effects were rather minimal in this case (i.e., the differences from the H, G model fit were small). Therefore, this implied that the phase-curve parameters derived previously were not biased by aspect effects.

As an additional use of the shape-based Hapke model, we searched for evidence of historical mass loss from the Didymos system via systematic brightening in the MPC data. Figures 1(c) and (d) show the model residuals as a function of observation date and heliocentric distance, respectively, which demonstrate that no historical brightening of Didymos occurred beyond the scatter of the data (i.e., rms residual of 0.35 mag). However, the immediate brightening of the Didymos system following the DART impact was apparent in the data, but it would have been difficult to distinguish from the large scatter without prior knowledge of the DART impact itself.

4. Thermophysical Properties

4.1. Thermophysical Modeling

Thermophysical modeling was performed for the Didymos system using the ATPM (Rozitis & Green 2011, 2012, 2013) in a configuration previously utilized for the binary asteroid (175706) 1996 FG3 (Wolters et al. 2011). In particular, the surface temperature distributions of the two bodies in the binary system were calculated independently of one another, and their thermal flux contributions were combined in the infrared data fitting. Wolters et al. (2011) previously determined this to be a suitable approximation because self-heating effects are small between the primary and secondary bodies, and eclipse shadows only occur relatively briefly. Therefore, the ATPM was run separately for Didymos and Dimorphos for each observation geometry using their respective DART-derived shape models (Barnouin et al. 2023; Daly et al. 2024).

For each facet of a given shape model, the ATPM solves the 1D heat conduction and surface boundary condition equations

given by

$$\frac{dT}{dt} = \frac{k}{\rho C_p} \frac{d^2T}{dz^2} \quad (7)$$

$$(1 - A_B) \left([1 - S(t)] \psi(t) \frac{F_{\text{SUN}}}{r^2(t)} + F_{\text{SCAT}}(t) \right) + F_{\text{RAD}}(t) + k \left(\frac{dT}{dz} \right)_{z=0} - \epsilon_B \sigma T_{z=0}^4 = 0, \quad (8)$$

respectively, where T is temperature, t is time, and z is depth (Rozitis et al. 2020b). In Equation (8), the functions $S(t)$, $\psi(t)$, $r(t)$, $F_{\text{SCAT}}(t)$, and $F_{\text{RAD}}(t)$ calculate shadowing, cosine of illumination angle, heliocentric distance, multiple-scattered sunlight, and self-heating, respectively. These functions are evaluated for each facet using the geometrical calculations described in Rozitis & Green (2011, 2012, 2013) with the asteroid ephemeris retrieved from the JPL Horizons System. Additionally, A_B is the Bond albedo, F_{SUN} is the integrated solar flux at 1 au (1367 W m^{-2}), ϵ_B is the bolometric emissivity, and σ is the Stefan-Boltzmann constant. Unresolved surface roughness is incorporated by adding a fractional coverage, f_R , of spherical-section craters to each shape-model facet upon which Equations (7) and (8) are also applied to each crater sub-facet. Here, we utilized hemispherical craters constructed from 100 sub-facets, and therefore the rms surface slope in degrees is given by $\theta = 49 f_R^{1/2}$.

To model diurnal temperature variations, Equation (7) is solved using a finite difference method with 650 time steps per rotation and 56 depth steps per eight diurnal skin depths, and Equation (8) is solved using a series of Newton-Raphson iterations. If seasonal temperature variations are also to be considered, then the depth profile can be extended by another 56 depth steps per eight seasonal skin depths. For specified input properties, the ATPM is initialized with time-averaged temperatures and iterated until surface temperatures converge to within 10^{-3} K between consecutive iterations.

For modeling the Didymos system thermal emission, we applied the ATPM to the DART-derived shape models of Didymos and Dimorphos (Barnouin et al. 2023; Daly et al. 2024), which were each decimated to 3072 facets using MeshLab (Cignoni et al. 2008) to improve the computational performance of the ATPM. As summarized in Table 3, we adopted a rotation period of 2.26 hr for Didymos, and assumed that the rotation period of Dimorphos was tidally locked with its pre-impact orbital period of 11.92 hr (Thomas et al. 2023). Similarly, we also assumed that the individual rotation poles were aligned with the binary orbit pole of $\lambda_p = 310.0^\circ$ and $\beta_p = -80.7^\circ$ (Naidu et al. 2023). Furthermore, we assumed a Bond albedo of 0.07 (i.e., that previously derived in Section 3.2), bolometric and spectral emissivity of 0.9 (i.e., a typical value adopted for S-type asteroids; Müller et al. 2005, 2014; Rozitis 2017), and thermal inertia in the range of $0\text{--}1000 \text{ J m}^{-2} \text{ K}^{-1} \text{ s}^{-1/2}$.

After the model surface temperatures were computed, the total model thermal flux was evaluated by summing the individual flux contributions from all facets and crater sub-facets visible to the observer. For individual facet i , the model

Table 3
Input and Derived Parameters for Thermophysical Modeling of the Didymos System

Parameter Group	Parameter	Value	References
Size and shape	Didymos size (m)	730 ± 17	Barnouin et al. (2023)
	Didymos shape (m × m × m)	819 × 801 × 605	
	Dimorphos pre-impact size (m)	150.0 ± 2.5	Daly et al. (2024)
	Dimorphos pre-impact shape (m × m × m)	177 × 168 × 114	
Optical	Absolute magnitude	18.16 ± 0.06	This work; Kitazato et al. (2004)
	Phase parameter	0.18 ± 0.04	
	Geometric albedo	0.17 ± 0.01	
	Bond albedo	0.07 ± 0.01	
Rotation	Didymos rotation period (hr)	2.260 0 ± 0.0001	Thomas et al. (2023)
	Dimorphos pre-impact orbital period (hr)	11.921 473 ± 0.000044	
	Rotation pole (°)	$\lambda_P = 310.0 \pm 3.0$ $\beta_P = -80.7 \pm 0.5$	Naidu et al. (2023)
	Obliquity (°)	167.7 ± 0.5	
Heliocentric orbit	Semimajor axis (au)	1.643	JPL Solution 205
	Eccentricity	0.383	
	Inclination (°)	3.414	
	Ascending node (°)	72.992	
	Argument of periapsis (°)	319.556	
	Yarkovsky semimajor axis drift (m yr ⁻¹)	-54.6 ± 3.5	
Thermophysical properties	Bolometric and spectral emissivity	0.9	Assumed
	Pre-impact thermal inertia (J m ⁻² K ⁻¹ s ^{-1/2})	320 ± 70 (VLT VISIR)	This work
	Post-impact thermal inertia (J m ⁻² K ⁻¹ s ^{-1/2})	260 ± 30 (JWST MIRI) 290 ± 50 (JWST NIRSpec)	Rivkin et al. (2023)
	Thermal roughness (° rms slope)	40 ± 3	This work
Mass	Bulk density (kg m ⁻³)	2550 ± 330 (constant TI) 2750 ± 350 (variable TI)	This work
	Mass (10 ¹¹ kg)	5.2 ± 0.4 (constant TI) 5.6 ± 0.4 (variable TI)	This work

flux at wavelength λ , $F_{\text{MOD},i}(\Gamma, \lambda, t)$, is given by

$$F_{\text{MOD},j}(\Gamma, \lambda, t) = B(\lambda, T_i(\Gamma, t))\varepsilon(\lambda)\frac{A_i v_i}{\Delta^2} \cos(e), \quad (9)$$

where $B(\lambda, T_i(\Gamma, t))$ is the Planck function, $\varepsilon(\lambda)$ is the spectral emissivity, A_i is the area of the facet, e is the emission angle, and v_i and Δ give the visibility and distance to the observer, respectively. Here, $T_i(\Gamma, t)$ is the temperature of the facet calculated by the ATPM for thermal inertia Γ at time t . For a specified body, the thermal flux, $F_{\text{BODY}}(\Gamma, \lambda, t)$, is then given by

$$F_{\text{BODY}}(\Gamma, f_R, \lambda, t) = \sum_{i=1}^{N_{\text{FACET}}} \left((1 - f_R) F_{\text{MOD},i}(\Gamma, \lambda, t) + f_R \sum_{j=1}^{100} F_{\text{MOD},j}(\Gamma, \lambda, t) \right), \quad (10)$$

where Γ and f_R can be unique values for each body. Finally, the total model flux from both Didymos and Dimorphos, $F_{\text{TOTAL}}(\Gamma, f_R, \lambda, t)$, is given by

$$F_{\text{TOTAL}}(\Gamma, f_R, \lambda, t) = \left(\frac{D_{\text{DIDY}}}{D_{\text{DIDY},0}} \right)^2 F_{\text{DIDY}}(\Gamma, f_R, \lambda, t) + \left(\frac{D_{\text{DIMO}}}{D_{\text{DIMO},0}} \right)^2 F_{\text{DIMO}}(\Gamma, f_R, \lambda, t), \quad (11)$$

where D_{DIDY} and D_{DIMO} are the adjustable diameters of Didymos and Dimorphos, respectively, and $D_{\text{DIDY},0}$ and $D_{\text{DIMO},0}$ are the sizes of their shape models that were used in the thermophysical modeling.

To derive the best-fitting properties, the model fluxes were compared against the infrared data, $F_{\text{OBS},n}(\lambda)$ and $\sigma_{\text{OBS},n}(\lambda)$, by minimizing the reduced- χ^2 given by

$$\chi_R^2 = \frac{1}{\nu} \sum_{n=1}^{N_{\text{OBS}}} \left(\frac{F_{\text{OBS},n}(\lambda) - F_{\text{TOTAL}}(\Gamma, f_R, \lambda, t)}{\sigma_{\text{OBS},n}(\lambda)} \right)^2, \quad (12)$$

where ν was the number of degrees of freedom in the fit (i.e., the number of data points minus the number of fitted parameters). As described in the next subsection, the fit uncertainties were quantified by Monte Carlo sampling rather than by reduced- χ^2 contours to effectively propagate the uncertainties of the input physical properties of a two-body system.

4.2. Analysis and Results

For the determination of thermal inertia and thermal roughness, we fitted the ATPM to just the infrared photometry to avoid biasing the results toward the September data if its spectrum was also included in the fit. We also rotationally averaged the model flux from Didymos and Dimorphos because the expected light-curve variations (Pravec et al. 2022) were similar to or less than the uncertainties in our measured infrared fluxes (i.e., ~4%–11%). Similarly, eclipse

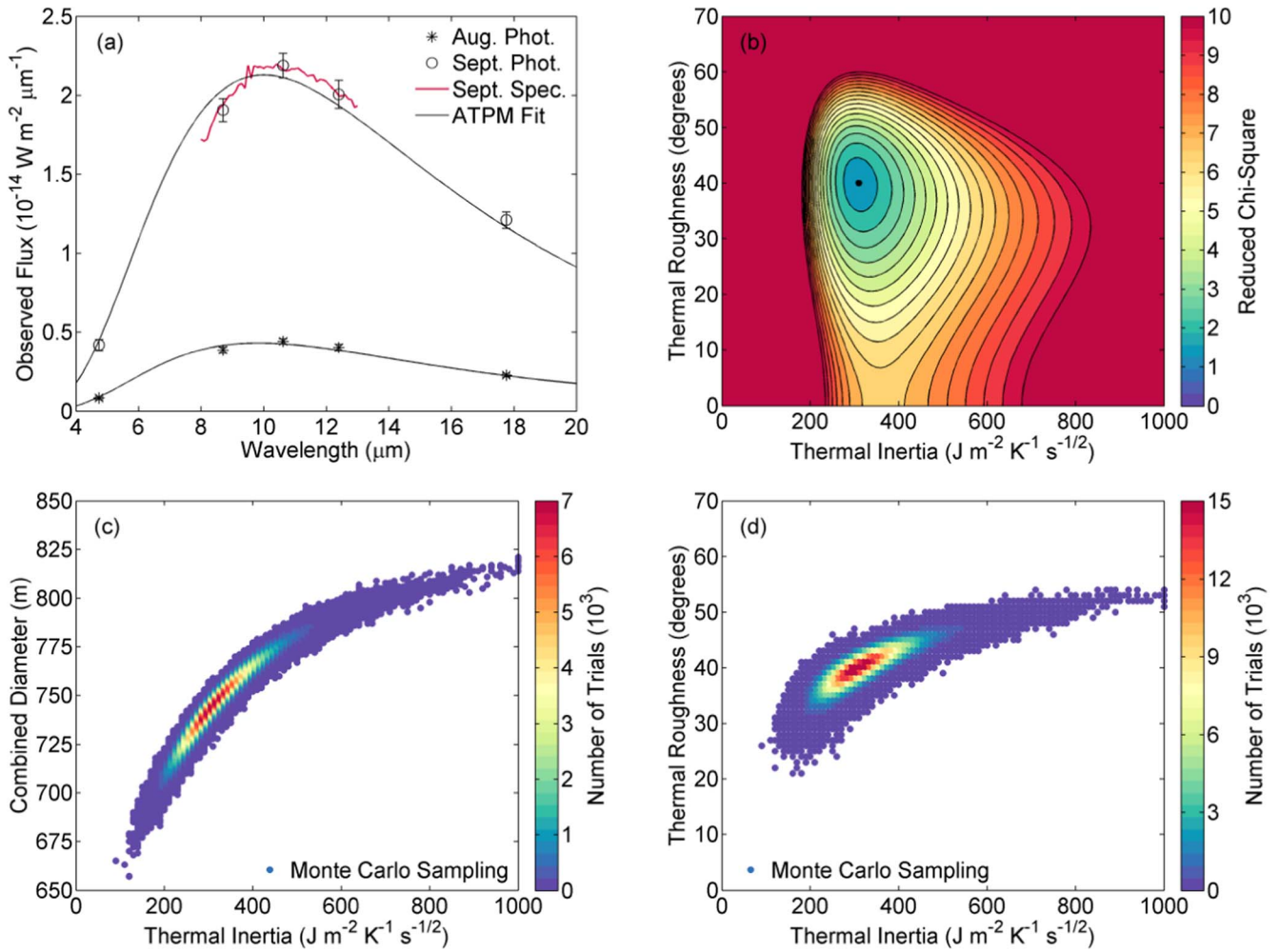


Figure 2. Thermal-infrared observations and thermophysical modeling of the Didymos system. (a) Mid-infrared photometry and spectroscopy acquired by the VLT telescope prior to the DART impact. The average fluxes are shown for each wavelength, and the best-fit continua determined by the ATPM are shown for comparison. Here, Dimorphos contributes $\sim 5\%$ to the total observed flux. (b) Example reduced- χ^2 contour plot showing the best-fit thermophysical solution when the diameters of Didymos and Dimorphos are held constant at their nominal values. (c) Two-dimensional histogram demonstrating the co-variance between the combined diameter and best-fit thermal inertia resulting from Monte Carlo sampling of the diameter uncertainties. (d) Two-dimensional histogram of the best-fit thermal inertia and thermal roughness resulting from Monte Carlo sampling of the input physical properties and mid-infrared data.

and/or occultation events, which have predicted amplitudes of $\sim 3\%$ – 5% in the optical (Scheirich & Pravec 2022), were not apparent in our data. Although there were predicted events during the observing period on both nights, these were eclipses (but not occultations) where nonzero thermal inertia would result in smaller amplitude variations in the thermal infrared. Therefore, for simplicity, we summed the rotationally averaged model flux from both bodies using Equation (11).

Figure 2(a) demonstrates the ATPM fit to the infrared data, and Figure 2(b) provides the reduced- χ^2 minimization grid for fixed diameters of Didymos and Dimorphos (i.e., they were held constant at their nominal shape model derived values; Table 3). This fit produced a reduced- χ^2 value of 1.68 and tightly constrains both the thermal inertia and thermal roughness. Here, the combination of low and high phase angle data (Table 2) allowed us to break the typical degeneracy between thermal inertia and thermal roughness. To quantify the fit uncertainties, we performed Monte Carlo random sampling of the uncertainties in the respective diameter estimates of Didymos and Dimorphos, and of the infrared fluxes, using one million trials. The reduced- χ^2 minimization was then repeated for each random trial to derive distributions of best-fitting thermal inertia and thermal roughness,

which are shown in Figures 2(c) and (d). The accumulated Monte Carlo trials result in a thermal inertia of $320 \pm 70 \text{ J m}^{-2} \text{K}^{-1} \text{s}^{-1/2}$ (i.e., mean value and standard deviation) and a thermal roughness of $40^\circ \pm 3^\circ$ rms slope (i.e., 0.67 ± 0.10 in terms of crater roughness fraction) for the Didymos system.

As shown in Figure 2(c), we found a strong co-variance between the best-fit thermal inertia and the combined effective diameter of Didymos and Dimorphos. In particular, a smaller-than-nominal combined diameter leads to a lower thermal inertia, and a larger-than-nominal combined diameter leads to a higher thermal inertia. This co-variance explains why we obtained a higher thermal inertia estimate of $530 \pm 140 \text{ J m}^{-2} \text{K}^{-1} \text{s}^{-1/2}$ in preliminary work (Rozitis et al. 2023), as the first size estimates of the Didymos system were somewhat larger than that determined in later refined analysis (i.e., $0.776 \pm 0.026 \text{ km}$ in Daly et al. 2023 versus $0.745 \pm 0.017 \text{ km}$ in Barnouin et al. 2023 and Daly et al. 2024). If the size of the Didymos system was to be refined again in future work, then we would expect the thermal inertia to change accordingly with this co-variance.

In our models, Dimorphos contributed $\sim 5\%$ and $\sim 4\%$ to the total observed flux during the August and September observations, respectively. We performed a three-parameter fit to the data

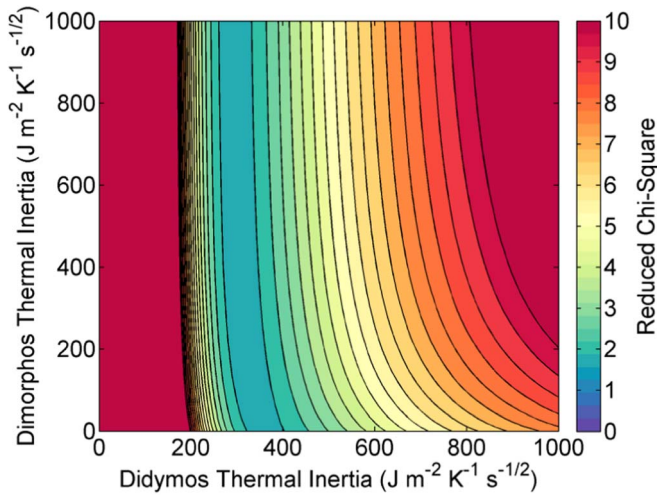


Figure 3. Reduced- χ^2 contour plot showing the best-fit solutions when the thermal inertia of Dimorphos is also introduced as an additional free parameter to that of Didymos. Here, the diameters of Didymos and Dimorphos have been held constant at their central values. As demonstrated, the mid-infrared data do not provide any constraints on the thermal inertia of Dimorphos.

(i.e., Didymos thermal inertia, Dimorphos thermal inertia, and system thermal roughness) to investigate whether the thermal inertia of Dimorphos could be distinguished from that of Didymos. Figure 3 demonstrates that there was no constraint on the thermal inertia of Dimorphos, but allowing it to vary did slightly increase the range of possible values for Didymos. Therefore, the thermal inertia of the two bodies could be quite different from one another, but we are unable to constrain any differences from this set of data. Furthermore, Figure 4 shows the model fit residuals as a function of observation time, and it confirms that we did not conclusively resolve any light-curve and/or eclipse features from either body. For instance, the scatter in the fit residuals ($\sim 6\%$) was comparable to the average flux uncertainty ($\sim 5\%$), which were both much too large to resolve expected temporal flux variations from the Didymos system.

As shown in Figures 2(a) and 4, the 8–13 μm infrared data appeared to show a different color temperature to the ATPM fit. It was initially ambiguous as to whether the temperature of the Didymos system was cooler than that predicted by the ATPM and/or if there was a spectral emissivity feature that was masquerading as a lower temperature. To investigate, we produced an emissivity spectrum of the Didymos system by dividing the photometric and spectral data by the best ATPM and NEATM (near-Earth asteroid thermal model; Harris 1998) fits. As shown in Figure 5, the emissivity spectrum of the Didymos system exhibits a sharp drop-off in spectral emissivity at wavelengths $< 9 \mu\text{m}$, which appears not to be a model artifact given that it is present in both the ATPM and NEATM fits. It also persisted when testing with an alternative bolometric and spectral emissivity value of 0.95 (i.e., the value derived for Bennu; Rozitis et al. 2020b). A search through the literature identified that the S-type asteroids (6) Hebe (Green et al. 1985) and (951) Gaspra (Vernazza et al. 2010) also exhibited similar spectral emissivity features, which are shown for comparison in Figure 5. Therefore, we concluded that this feature was likely real and that we should not try to overfit it with the ATPM.

The 5–20 μm infrared data acquired post-impact by the James Webb Space Telescope (JWST) also shows a 7 μm emissivity minimum (Rivkin et al. 2023), but the $< 9 \mu\text{m}$ drop-off was not as extreme as that seen in this work. However, Rivkin et al.

(2023) also identified many examples in the literature of laboratory meteorite spectra that show very extreme drop-offs in the $< 9 \mu\text{m}$ spectral emissivity (e.g., Bramble et al. 2021a, 2021b). Therefore, it was not clear whether the subtle differences in this feature were caused by spatial variations in composition/particle size and/or by differences in the observational circumstances, as such emissivity features are also known to be rather sensitive to the illumination and observation conditions in laboratory studies (e.g., Maturilli et al. 2016).

5. The Yarkovsky Effect

5.1 Orbital Drift Modeling

The Yarkovsky effect of the Didymos system can be evaluated by running a thermophysical model around its heliocentric orbit and integrating the photon recoil forces that arise from the modeled thermal emission. In particular, the photon recoil force acting on facet i , $\mathbf{p}_i(\Gamma, t)$, is given by

$$\mathbf{p}_i(\Gamma, t) = -\frac{2A_i \epsilon_B \sigma T_i^4(\Gamma, t)}{3c} \mathbf{n}_{\text{EFF},i}(t), \quad (13)$$

where A_i and $\mathbf{n}_{\text{EFF},i}$ are the facet area and effective normal, respectively, and c is the speed of light (Rozitis & Green 2012, 2013). The overall force acting on a specified body, $\mathbf{P}_{\text{BODY}}(\Gamma, f_R, t)$, can be calculated using

$$\mathbf{P}_{\text{BODY}}(\Gamma, f_R, t) = \sum_{i=1}^{N_{\text{FACETS}}} \left((1 - f_R) \mathbf{p}_i(\Gamma, t) + f_R \sum_{j=1}^{100} \mathbf{p}_j(\Gamma, t) \right), \quad (14)$$

and the total force acting on the Didymos system barycenter, $\mathbf{P}_{\text{TOTAL}}(\Gamma, f_R, t)$, is given by

$$\mathbf{P}_{\text{TOTAL}}(\Gamma, f_R, t) = \left(\frac{D_{\text{DIDY}}}{D_{\text{DIDY},0}} \right)^2 \mathbf{P}_{\text{DIDY}}(\Gamma, f_R, t) + \left(\frac{D_{\text{DIMO}}}{D_{\text{DIMO},0}} \right)^2 \mathbf{P}_{\text{DIMO}}(\Gamma, f_R, t). \quad (15)$$

For simplicity, this total force can be rotationally averaged, and the change in orbital energy ΔE is then given by

$$\Delta E = \sum_{n=1}^{N_{\text{ORB}}} (v_{x,n} P_{x,n} + v_{y,n} P_{y,n} + v_{z,n} P_{z,n}) \Delta t_n, \quad (16)$$

where v_d are the orbital velocity components in the directions of the P_d force components, and Δt is the orbital time step for N_{ORB} steps. Finally, the rate of change in orbital semimajor axis, da/dt , is given by

$$\frac{da}{dt} = \frac{2a^2}{P_{\text{ORB}} G M_{\text{SUN}} M_{\text{AST}}} \Delta E, \quad (17)$$

where a is the semimajor axis, P_{ORB} is the orbital period, G is the gravitational constant, and M_{SUN} and M_{AST} are the masses of the Sun and the Didymos system, respectively. Equation (17) can be re-arranged to estimate the Didymos system mass from an orbital drift measurement, which can then be used to estimate the system bulk density utilizing the shape model volumes.

This parameterization allows uncertainties in the input parameters to be propagated through to the calculated orbital drift and bulk density, which can be assessed through both

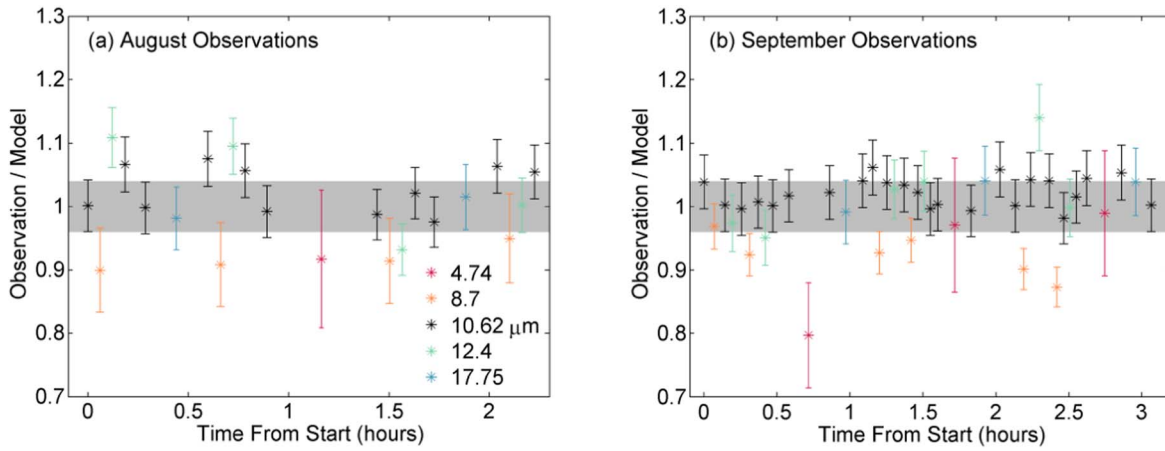


Figure 4. Residuals of the ATPM fit to the (a) August and (b) September mid-infrared photometry as a function of observation time. The shaded gray area indicates the level of flux variability expected from the Didymos system, as inferred from optical light curves (Pravec et al. 2022; Scheirich & Pravec 2022). The observation start times including light-time corrections were 59815.26401 and 59848.18858 in Modified Julian Date (MJD), respectively.

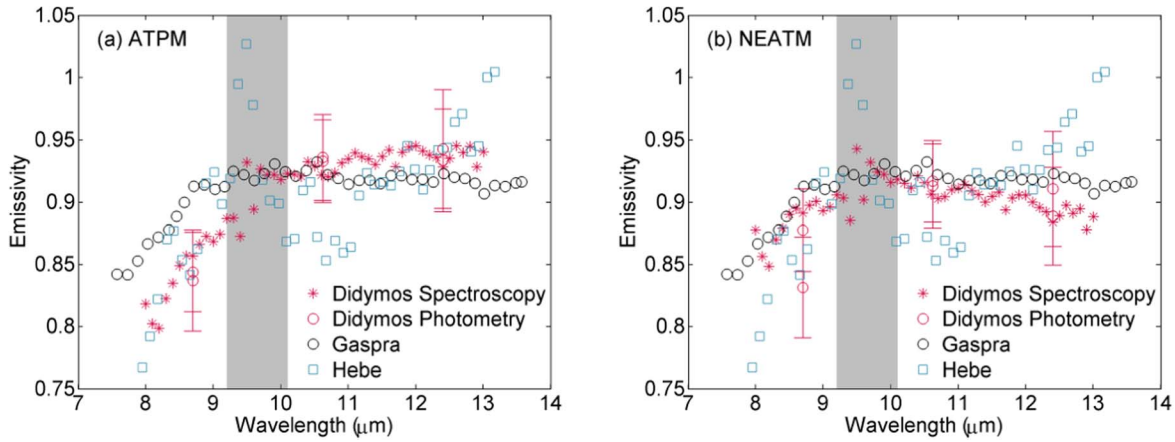


Figure 5. Spectral emissivity of the Didymos system derived by the (a) ATPM and (b) NEATM. The emissivity spectra of the S-type asteroids (6) Hebe (Green et al. 1985) and (951) Gaspra (Vernazza et al. 2010) are shown for comparison, as they also exhibit a sharp drop-off in spectral emissivity at wavelengths $<9 \mu\text{m}$. The shaded gray area indicates a region of strong telluric absorption, which introduces additional noise into the derived spectra. The error bars give the standard errors for the mean spectral emissivity values derived from the infrared photometry.

systematic and Monte Carlo sampling. As an additional option, possible temperature-dependent thermal properties can also be incorporated by allowing the thermal inertia to vary with heliocentric distance according to

$$\Gamma(r) = \Gamma_0 \left(\frac{r}{r_0} \right)^\xi, \quad (18)$$

where Γ_0 is the thermal inertia measured at heliocentric distance r_0 , and ξ is an exponent that specifies the degree of thermal inertia variation (Rozitis et al. 2018).

5.2 Analysis and Results

The ephemeris for the Didymos system produces a Yarkovsky orbital drift of $-54.6 \pm 3.5 \text{ m yr}^{-1}$ (JPL Solution 205¹¹), which we used to estimate the bulk density from model-to-measurement comparisons. Here, we propagated the results from the Monte Carlo analysis of the infrared observations described in Section 4.2 by assuming that either the thermal

inertia remains constant during the Didymos orbit, or that it varies with heliocentric distance due to temperature-dependent thermal properties. For the temperature-dependent case, we adopted a heliocentric distance exponent ξ of -0.75 because such a dependence is expected from a $\sim T^3$ dependence of radiative thermal conductivity for a particulate regolith (Delbo et al. 2007; Rozitis et al. 2018). Furthermore, in each Monte Carlo trial, we also randomly sampled the uncertainty of the Yarkovsky measurement to fully quantify the uncertainty on the derived bulk density.

Figure 6(a) shows the bulk density of the Didymos system derived as a function of thermal inertia, and Figure 6(b) shows the distributions of derived bulk density. As indicated, the accumulated Monte Carlo trials result in bulk densities of 2550 ± 330 and $2750 \pm 350 \text{ kg m}^{-3}$ for constant and temperature-dependent thermal properties, respectively. Here, Dimorphos contributed $\sim 5\%$ to the total Yarkovsky force acting on the Didymos system, and the $\sim 8\%$ enhancement caused by temperature-dependent properties was consistent with that obtained in simulations performed for other asteroids (e.g., Hanuš et al. 2018b; Rozitis et al. 2018). Figure 7 demonstrates that this small temperature-dependent enhancement was primarily caused

¹¹ https://ssd.jpl.nasa.gov/ftp/eph/small_bodies/dart/didymos/didymos_s205.pdf

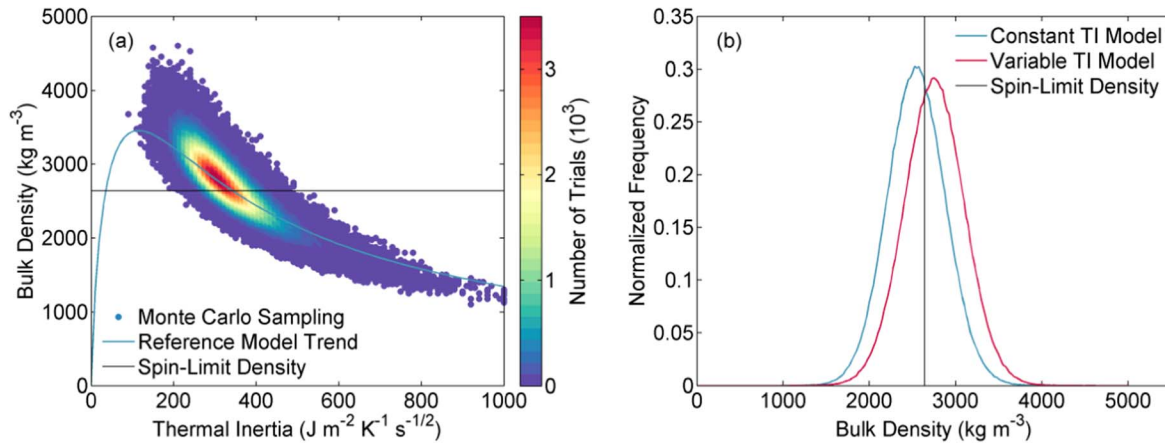


Figure 6. Bulk density of the Didymos system derived from model-to-measurement comparisons of its Yarkovsky orbital drift. (a) Two-dimensional histogram of bulk density derived from Monte Carlo sampling of the input thermophysical properties and measured Yarkovsky orbital drift. The reference model trend gives the bulk density derived as a function of thermal inertia when the other input properties have been held constant. (b) Bulk density distributions derived if either the thermal inertia (TI) remains constant or varies during the eccentric heliocentric orbit of Didymos. In both panels, the spin-limit density ($\sim 2640 \text{ kg m}^{-3}$) indicates the bulk density at which self-gravity balances equatorial centrifugal forces for the Didymos primary body.

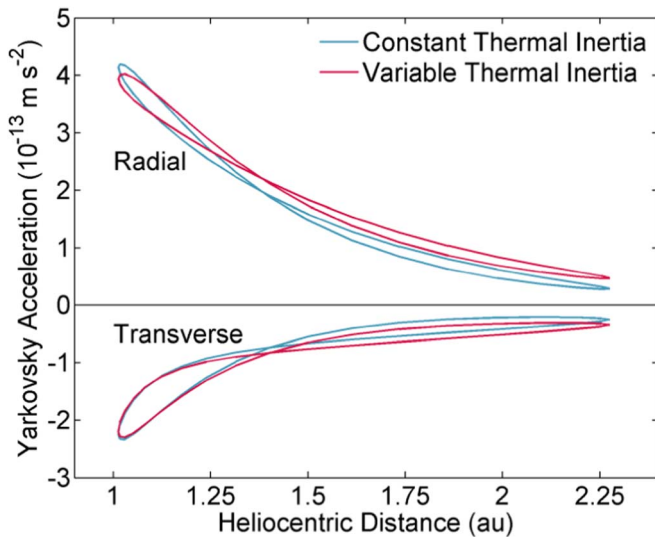


Figure 7. Yarkovsky effect induced accelerations of the Didymos system as a function of heliocentric distance. The radial component gives the acceleration directed along the Sun-asteroid vector, and the transverse component gives the acceleration directed along the vector perpendicular to the radial vector in the direction of the asteroid velocity. The constant thermal inertia accelerations assume a constant value of $320 \text{ J m}^{-2} \text{ K}^{-1} \text{ s}^{-1/2}$ around the Didymos orbit, and the variable thermal inertia accelerations assume it varies with heliocentric distance according to Equation (18) with an exponent ξ of -0.75 . Both acceleration profiles have been computed assuming a bulk density of 2750 kg m^{-3} .

by enhancements to the Yarkovsky effect induced accelerations at large heliocentric distance.

These bulk density estimates are in good agreement with the independent estimates of 2400 ± 300 (Daly et al. 2023) and 2800 ± 280 (Barnouin et al. 2023; Naidu et al. 2023) kg m^{-3} determined from analysis of the binary mutual orbit, and they validate the model implemented here. The bulk density estimates also overlap with the value at which self-gravity balances equatorial centrifugal forces for the current shape model and spin-rate of Didymos (i.e., $\sim 2640 \text{ kg m}^{-3}$), as calculated from a polyhedron gravity model modified to include rotational centrifugal forces (Werner & Scheeres 1996; Rozitis et al. 2014).

6. Discussion

6.1 Thermal Inertia Interpretation and Implications for the DART Impact

In comparison to other S-type near-Earth asteroids visited by spacecraft, the thermal inertia of $320 \pm 70 \text{ J m}^{-2} \text{ K}^{-1} \text{ s}^{-1/2}$ derived for Didymos is between that determined previously for the asteroids (433) Eros ($150 \pm 50 \text{ J m}^{-2} \text{ K}^{-1} \text{ s}^{-1/2}$; Mueller 2012; Rozitis 2017) and (25143) Itokawa ($700 \pm 200 \text{ J m}^{-2} \text{ K}^{-1} \text{ s}^{-1/2}$; Müller et al. 2005, 2014). This implies that the surface morphology of Didymos is perhaps intermediate between those two asteroids (Figure 8). In particular, the surface of Eros is dominated by a tens of meters deep regolith layer consisting of $\sim 2 \text{ mm}$ particles (Veveřka et al. 2001; Gundlach & Blum 2013), and has multiple boulders and craters where many are also partially buried in regolith (Robinson et al. 2002). In contrast, the surface of Itokawa is densely populated by meter-to-decameter sized boulders and lacks distinctive craters (Saito et al. 2006), but it does have a central “sea” where millimeter- to centimeter-sized regolith particles have accumulated in a local gravitational low (Yano et al. 2006).

At first glance, the images returned by DART prior to impact (Barnouin et al. 2023; Daly et al. 2023) do seem to show that the surface of the primary body Didymos is intermediate between that of Eros and Itokawa (Figure 8). There are unresolved smooth terrains on and near the equator (reminiscent of Eros), and there are meter-to-decameter sized boulders at mid-to-high latitudes (reminiscent of Itokawa). For the secondary body Dimorphos, the high-resolution images reveal a surface densely populated with meter-sized boulders, and one would expect Dimorphos to have a high thermal inertia comparable to that of Itokawa. However, we are unable to uniquely constrain the thermal inertia of Dimorphos due to its small flux contribution (Figure 3), but it is possible that its thermal inertia is different to that of Didymos within the constraints of our data.

In terms of physical interpretation, this thermal inertia is moderately low given that analogous meteorites have a value of $\sim 2000 \text{ J m}^{-2} \text{ K}^{-1} \text{ s}^{-1/2}$ (Gundlach & Blum 2013), which means that it can be interpreted in terms of either a small particle size (Gundlach & Blum 2013; Sakatani et al. 2017) and/or a high rock porosity (Grott et al. 2019; Sakatani et al.



Figure 8. Spacecraft resolved images (not all to scale) of the S-type near-Earth asteroids (433) Eros (left), (25143) Itokawa (top right), and (65803) Didymos/Dimorphos (bottom right). These asteroids have thermal inertia values of 150 ± 50 (Mueller 2012; Rozitis 2017), 700 ± 200 (Müller et al. 2005; Müller et al. 2014), and 320 ± 70 (this work) $\text{J m}^{-2} \text{K}^{-1} \text{s}^{-1/2}$, respectively. For the Didymos/Dimorphos composite image (bottom right), Dimorphos (smaller body) is shown at a higher resolution than Didymos (larger body), their north poles are oriented upwards, and their relative sizes and the distance between them are drawn to scale (Daly et al. 2023). Image credit NASA and JAXA.

2021). It is possible to distinguish between the two cases by measuring any changes in thermal inertia with heliocentric distance (Rozitis et al. 2018, 2020b). For instance, the thermal inertia of particulate regolith should vary with heliocentric distance according to Equation (18) while that of porous rocks and boulders should remain approximately constant (i.e., for Bennu it was determined that the exponent $|\xi| < 0.25$; Rozitis et al. 2020b). Unfortunately, our infrared data were acquired at approximately the same heliocentric distance (Table 2) and do not constrain any changes in the thermal inertia. However, the thermal inertia of the Didymos system would be expected to vary from $180 \pm 40 \text{ J m}^{-2} \text{K}^{-1} \text{s}^{-1/2}$ at aphelion to $340 \pm 80 \text{ J m}^{-2} \text{K}^{-1} \text{s}^{-1/2}$ at perihelion if it had an exponent ξ of -0.75 .

Including this hypothetical thermal inertia variation in the Yarkovsky effect modeling did enhance the overall recoil force by $\sim 8\%$, but the uncertainties on the measurements for the orbital drift and bulk density of the Didymos system did not allow us to confirm it. However, Cambioni et al. (2021) argued that the surfaces of S-type asteroids are readily able to produce particulate regolith from thermal cracking and micrometeorite bombardment, and so the particle size interpretation is perhaps more relevant in this case anyway. Therefore, this thermal inertia measurement translates to a mean particle size of $\sim 2\text{--}7 \text{ mm}$ (Rivkin et al. 2023), and we adopt $2750 \pm 350 \text{ kg m}^{-3}$ for the bulk density that was derived from modeling the Yarkovsky effect with heliocentric distance variations of thermal inertia included.

To complement this study, Rivkin et al. (2023) acquired infrared observations of Didymos with JWST approximately 2 months after the DART impact. In that study, they used an identical thermophysical model with data collected by the

MIRI (Mid-Infrared Instrument) and NIRSpec (Near Infrared Spectrograph) instruments to derive thermal inertia values of 260 ± 30 and $290 \pm 50 \text{ J m}^{-2} \text{K}^{-1} \text{s}^{-1/2}$ for Didymos, respectively. These values agree well within the respective uncertainties of the pre-impact value derived in this work, and in combination they indicate that the DART impact did not change the thermal inertia of the Didymos system.

A lack of change in the thermal inertia of Didymos following the DART impact was not necessarily unexpected given the amount of material that would have to be redistributed to make a noticeable change. For instance, a $\sim 1 \text{ mm}$ layer of fine dust was previously shown to significantly alter the apparent thermal inertia of an asteroid surface in numerical studies (Biele et al. 2019; Grott et al. 2019; Rozitis et al. 2020b). Such a global layer would require $\sim 5 \times 10^6 \text{ kg}$ of material to be redeposited, which is $\sim 10\%$ – 40% of the estimated mass that was observed to be ejected by the DART impact (i.e., $1.3\text{--}6.4 \times 10^7 \text{ kg}$; Roth et al. 2023). Furthermore, no permanent spectral changes were observed on Didymos (Polishook et al. 2023), which suggests that no system-wide resurfacing occurred at even thinner layers.

Finally, it is important to note that the VLT and JWST observations sampled slightly different latitudes of the Didymos system. As shown in Figure 9, the VLT observations primarily sampled the southern mid-latitudes of the two bodies while the JWST observations were primarily equatorial. It was previously hypothesized that small rapidly rotating asteroids should have a low thermal inertia equator, as regolith mobilized by seismic shaking would naturally migrate toward the equatorial gravitational low (Garcia et al. 2015). Furthermore, a sufficiently fast spin-rate could shed equatorial boulders by rotational centrifugal forces (Trógolo et al. 2023). The equator of Didymos appears smooth in imaging (Figure 8), but it was

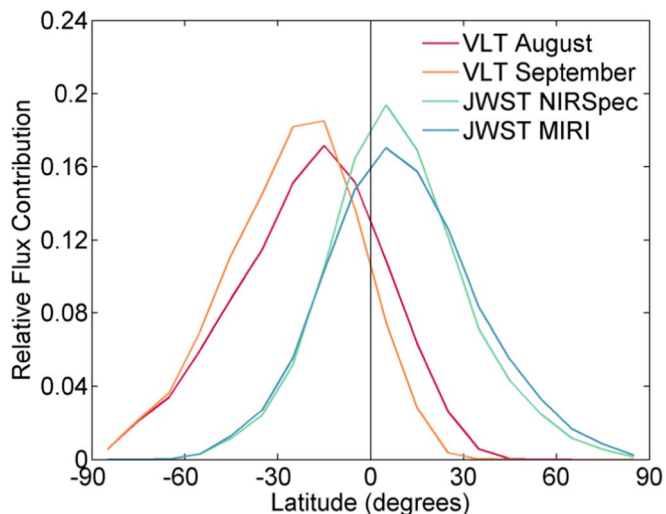


Figure 9. Latitude distributions of observed flux from the Didymos system for the pre-impact VLT (this work) and post-impact JWST (Rivkin et al. 2023) infrared observations.

unclear from the VLT and JWST observations whether it has a substantively different thermal inertia or not. The JWST thermal inertia is slightly lower, but it is within the uncertainty of the VLT result. Thermal inertia mapping by the upcoming ESA Hera mission would identify if any latitude banding is present on Didymos and also distinguish the value for Dimorphos (Michel et al. 2022; Okada et al. 2022).

6.2 Thermal Roughness Interpretation

The thermal roughness of $40^\circ \pm 3^\circ$ rms slope derived for Didymos is much higher than that of $\sim 20^\circ\text{--}35^\circ$ determined for the Moon (Rozitis & Green 2011; Bandfield et al. 2015; Müller et al. 2021), but it is consistent with the range of $\sim 30^\circ\text{--}50^\circ$ determined for other asteroids (Spencer 1990; Rozitis 2017; Rozitis et al. 2020b; Shimaki et al. 2020). For instance, it is most comparable to the thermal roughnesses of $40^\circ \pm 3^\circ$ and $47^\circ \pm 5^\circ$ derived for the asteroids Bennu and Ryugu, respectively. As previously mentioned, the thermal roughness of Bennu is driven by the shape and number density of rocks and boulders not resolved by the topography included in its thermophysical model (Rozitis et al. 2020b), and the high-resolution images of the surface of Dimorphos are somewhat reminiscent of Bennu’s roughest regions. This implies that the thermal roughness of the Didymos system is perhaps also driven by unresolved rocks, boulders, and surface undulations. For a thermal inertia of $320 \pm 70 \text{ J m}^{-2} \text{ K}^{-1} \text{ s}^{-1/2}$, the diurnal thermal skin depths of Didymos and Dimorphos are ~ 1 and ~ 2 cm, respectively, as calculated by assuming a bulk density of 2750 kg m^{-3} and a heat capacity of $550 \text{ J kg}^{-1} \text{ K}^{-1}$ (Opeil et al. 2010). Surface structures starting at these spatial scales would not be resolved in the shape models used for thermophysical modeling, as the facet sizes for Didymos and Dimorphos were ~ 33 and ~ 7 m, respectively. For future studies, the laser altimeter included on the upcoming ESA Hera mission will be capable of directly measuring surface roughness at the ~ 0.5 m scale (Michel et al. 2022), and therefore would provide meaningful insights into the thermal roughness measured here when considering the fractal-like nature of rough planetary surfaces (Shepard et al. 2001; Rozitis 2017).

6.3 Temperature Conditions and Ice Stability

To assist in the planning for the ESA Hera mission (Michel et al. 2022), and to investigate whether Didymos could host surface/subsurface water ice, we evaluated the surface and subsurface temperatures experienced throughout the orbit of Didymos. In particular, surface temperatures will be measured by the thermal-infrared imager (TIRI) developed by JAXA for the ESA Hera mission (Okada et al. 2022), and evidence for water ice within S-type near-Earth asteroids has recently been increasing. For the latter, near-infrared observations have detected $3 \mu\text{m}$ features associated with water/OH on eight S-type near-Earth asteroids (Rivkin et al. 2018; McGraw et al. 2022), and laboratory analysis finds small abundances of water within samples returned from Itokawa (Chan et al. 2021). Furthermore, the identification of asteroids with anomalously large nongravitational accelerations or “dark comets” indicates the presence of reservoirs of water ice (or other volatile materials) within unexpected planetary bodies (Farnocchia et al. 2023; Seligman et al. 2023), which raises questions as to whether weak cometary-like activity could contribute to the orbital drift of the Didymos system.

For this investigation, the orbital temperature variations were computed using similar methods to those described in Rozitis et al. (2020a) for Bennu, but we included the additional effects of the Didymos seasonal thermal wave due to its significant nonperpendicular obliquity. Figures 10(a) and (b) show the distribution of maximum surface temperatures experienced by each facet at any point during the heliocentric orbit of Didymos, and Figures 10(c) and (d) show the orbit-averaged temperatures that are characteristic of the deep subsurface conditions. As shown, these temperatures were much too warm for surface water ice to be stable for any length of time, but subsurface ice was potentially stable over geologic timescales at the poles of Didymos. In particular, $57,000\text{--}78,000 \text{ m}^2$ of the polar regions of Didymos (predominantly the south pole) or 3.3%–4.5% of the total surface area have orbit-averaged temperatures that are below 145 K, where buried water ice could be stable for up to $\sim 10^9$ yr (Schorghofer 2008).

The presence of any water ice within Didymos depends strongly on its past dynamical history, as its orbit, spin state, and surface are expected to have evolved with time. However, Schorghofer et al. (2020) showed that it is possible for a near-Earth asteroid to have retained polar water ice during its migration from the main belt, and Statler (2015) demonstrated that the obliquity component of the YORP effect rapidly moves the spin-axes of kilometer-sized asteroids into orbit-perpendicular configurations that facilitate the polar stability of water ice (i.e., within $\sim 10^5$ yr).

If subsurface water ice was present in these polar regions, then it would have been undetectable by the JWST near-infrared observations because they primarily sampled the equatorial region (Figure 9; Rivkin et al. 2023). However, if this hypothetical ice was sublimating, then it is unlikely that it would have contributed significantly to the orbital drift of the Didymos system and its Yarkovsky-derived bulk density estimate. This is because the resulting recoil forces would be directed mostly perpendicular rather than parallel to the asteroid’s heliocentric orbital plane.

For completeness, Figures 10(e) and (f) show the minimum surface temperatures experienced by each facet on Didymos. Therefore, the characteristic temperatures of Didymos range

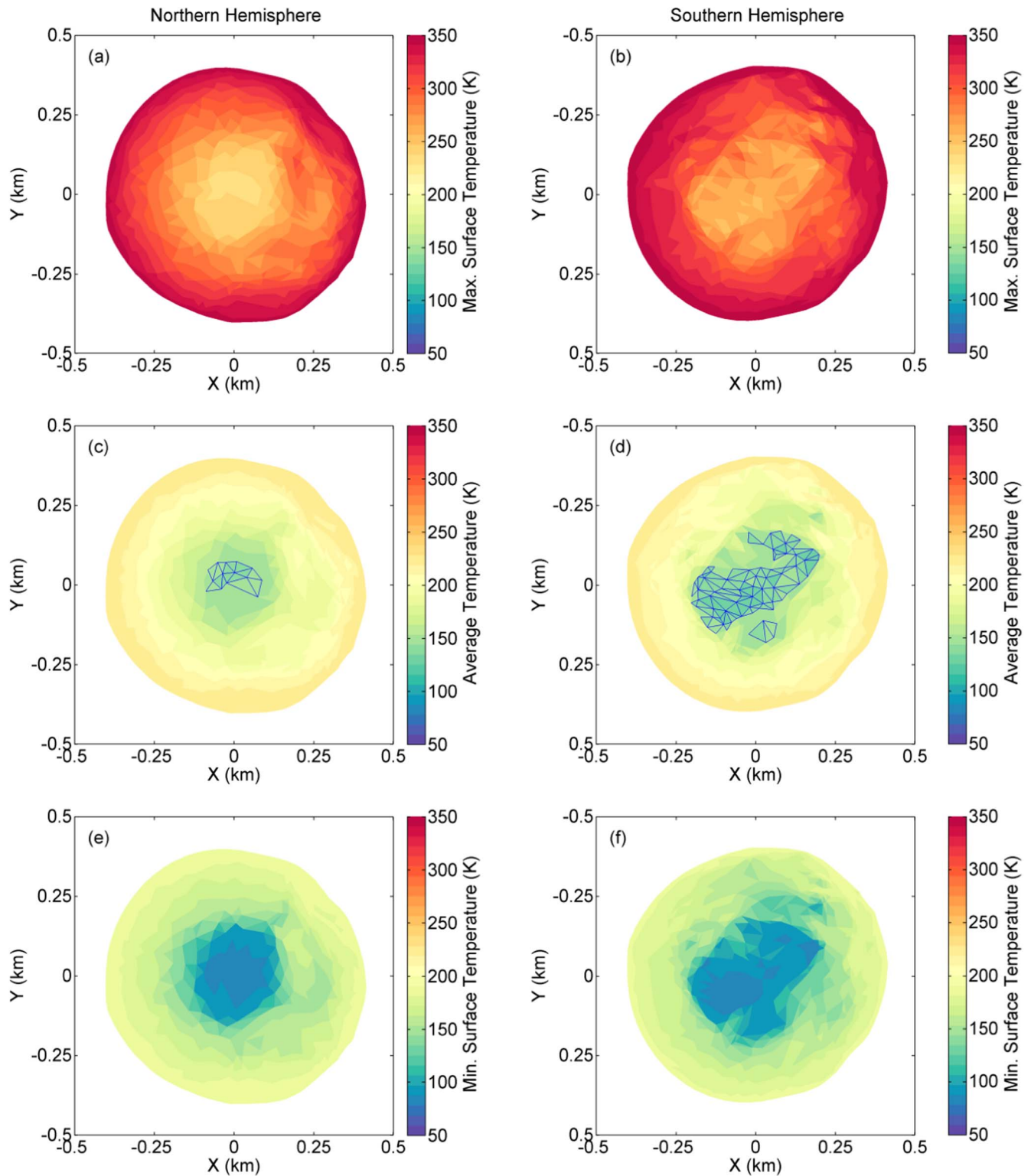


Figure 10. Global temperature distributions for the Didymos primary body. (a), (b) Maximum surface temperature attained at any point during its rotation and orbit. (c), (d) Time-averaged temperature computed from all rotations throughout its orbit. The highlighted facets have average temperatures below 145 K where subsurface water ice is potentially stable over geologic timescales if present. (e), (f) Minimum surface temperature attained at any point during its rotation and orbit. In all panels, the temperatures have been computed for the smooth surface model component assuming a thermal inertia of $320 \text{ J m}^{-2} \text{ K}^{-1} \text{ s}^{-1/2}$.

from 82 ± 4 to 350 ± 6 K, which would be measurable by the TIRI instrument on board the ESA Hera spacecraft (Okada et al. 2022). Spatial- and temporal-resolved temperature mapping by the ESA Hera mission would enable detailed

thermophysical models of Didymos and Dimorphos to be constructed for further investigation of their thermal properties, Yarkovsky effect, and of any potential cold traps for hosting surface/subsurface water ice.

7. Summary and Conclusions

From pre-impact observations acquired with the OU PIRATE and ESO VLT telescopes, we derived a Bond albedo of 0.07 ± 0.01 , a thermal inertia of $320 \pm 70 \text{ J m}^{-2} \text{ K}^{-1} \text{ s}^{-1/2}$, and a thermal roughness of $40^\circ \pm 3^\circ$ rms slope for the southern mid-latitudes of the Didymos system. It was not possible to uniquely constrain the thermal inertia of Dimorphos, but it is possible that it is different to that of Didymos within the constraints of our data. These properties are compatible with the ranges determined for other S-type near-Earth asteroids (Domingue et al. 2002; Delbo et al. 2015), and the thermal inertia is consistent with that of 260 ± 30 and $290 \pm 50 \text{ J m}^{-2} \text{ K}^{-1} \text{ s}^{-1/2}$ determined from post-impact observations acquired with the MIRI and NIRSpec instruments on the JWST telescope, respectively (Rivkin et al. 2023). Therefore, we conclude that the DART impact did not substantially change the thermal inertia of the Didymos system.

Thermophysical modeling of the Yarkovsky effect with these properties was used to derive a bulk density of $2750 \pm 350 \text{ kg m}^{-3}$ for the Didymos system, which agrees with the independent estimates of 2400 ± 300 (Daly et al. 2023) and 2800 ± 280 (Barnouin et al. 2023; Naidu et al. 2023) kg m^{-3} determined from analysis of the binary mutual orbit. These bulk density estimates also overlap with the value of $\sim 2640 \text{ kg m}^{-3}$ at which self-gravity balances equatorial centrifugal forces for the current shape model and spin-rate of Didymos.

Finally, the surface temperatures of Didymos range from 82 ± 4 to $350 \pm 6 \text{ K}$ during its orbit about the Sun, and $57,000\text{--}78,000 \text{ m}^2$ of its polar regions (3.3%–4.5% of the total surface area) have orbit-averaged temperatures that are below 145 K where buried water ice could be stable for up to $\sim 10^9$ yr if present. Surface temperature mapping by the upcoming ESA Hera mission will be used to investigate the thermophysical properties of the Didymos system in more detail (Michel et al. 2022; Okada et al. 2022).

Acknowledgments

This work was funded by the UK Science and Technology Facilities Council (STFC) and was based on observations performed at the ESO Paranal observatory in Chile (program ID 109.2373). This work was supported by the DART mission, NASA contract No. 80MSFC20D0004.

Appendix Additional Tables

We here include the mid-infrared data of Didymos collected by the ESO VLT before the DART impact. Table A1 lists the standard stars used for calibration of the VISIR instrument, and Tables A2 and A3 provide the mid-infrared photometry and spectrum of Didymos, respectively.

Table A1
Standard Stars Used for the ESO VLT VISIR Calibration

Standard Star	Observation Date	<i>M</i> Band (Jy)	J8.9 (Jy)	B10.7 (Jy)	B12.4 (Jy)	Q1 (Jy)
HD787	2022 Aug 24	26.3621	10.9159	8.2615	6.1426	3.0229
HD219784	2022 Aug 24	22.2917	9.2046	6.7326	4.9576	2.4663
HD12524	2022 Sep 26	31.9227	13.2185	10.0042	7.4377	3.6604
HD26967	2022 Sep 26	37.5168	15.4928	11.3329	8.3441	4.1515

Table A2
ESO VLT VISIR Photometry of Didymos

Observation Date (MJD)	Filter	Wavelength (μm)	Observed Flux ($\text{W m}^{-2} \mu\text{m}^{-1}$)	Flux Uncertainty ($\text{W m}^{-2} \mu\text{m}^{-1}$)
59815.26401	B10.7	10.62	4.304E-15	1.720E-16
59815.26652	J8.9	8.7	3.778E-15	2.768E-16
59815.26907	B12.4	12.4	4.312E-15	1.836E-16
59815.27166	B10.7	10.62	4.584E-15	1.853E-16
59815.27591	B10.7	10.62	4.293E-15	1.745E-16
59815.28234	Q1	17.75	2.220E-15	1.115E-16
59815.28887	B10.7	10.62	4.622E-15	1.882E-16
59815.29149	J8.9	8.7	3.818E-15	2.795E-16
59815.29409	B12.4	12.4	4.256E-15	1.745E-16
59815.29663	B10.7	10.62	4.542E-15	1.813E-16
59815.30112	B10.7	10.62	4.265E-15	1.732E-16
59815.31241	<i>M</i> - Band	4.74	8.196E-16	9.694E-17
59815.32396	B10.7	10.62	4.244E-15	1.717E-16
59815.32660	J8.9	8.7	3.844E-15	2.820E-16
59815.32923	B12.4	12.4	3.623E-15	1.592E-16
59815.33188	B10.7	10.62	4.389E-15	1.741E-16
59815.33586	B10.7	10.62	4.196E-15	1.711E-16
59815.34240	Q1	17.75	2.296E-15	1.158E-16
59815.34893	B10.7	10.62	4.574E-15	1.812E-16
59815.35152	J8.9	8.7	3.990E-15	2.933E-16
59815.35409	B12.4	12.4	3.897E-15	1.636E-16
59815.35668	B10.7	10.62	4.533E-15	1.824E-16
59848.18858	B10.7	10.62	2.225E-14	9.149E-16
59848.19155	J8.9	8.7	2.000E-14	7.280E-16
59848.19453	B10.7	10.62	2.146E-14	8.828E-16
59848.19666	B12.4	12.4	1.911E-14	8.666E-16
59848.19923	B10.7	10.62	2.134E-14	8.761E-16
59848.20154	J8.9	8.7	1.909E-14	6.935E-16
59848.20407	B10.7	10.62	2.157E-14	8.857E-16
59848.20614	B12.4	12.4	1.866E-14	8.458E-16
59848.20824	B10.7	10.62	2.144E-14	8.797E-16
59848.21277	B10.7	10.62	2.178E-14	8.943E-16
59848.21846	<i>M</i> - Band	4.74	3.625E-15	3.764E-16
59848.22444	B10.7	10.62	2.188E-14	8.982E-16
59848.22904	Q1	17.75	1.171E-14	5.986E-16
59848.23386	B10.7	10.62	2.228E-14	9.141E-16
59848.23677	B10.7	10.62	2.273E-14	9.323E-16
59848.23867	J8.9	8.7	1.914E-14	6.941E-16
59848.24075	B10.7	10.62	2.221E-14	9.116E-16
59848.24294	B12.4	12.4	2.015E-14	9.126E-16
59848.24566	B10.7	10.62	2.213E-14	9.086E-16
59848.24766	J8.9	8.7	1.956E-14	7.083E-16
59848.24957	B10.7	10.62	2.188E-14	8.997E-16
59848.25136	B12.4	12.4	2.041E-14	9.245E-16
59848.25316	B10.7	10.62	2.134E-14	8.761E-16
59848.25524	B10.7	10.62	2.148E-14	8.838E-16
59848.26011	<i>M</i> - Band	4.74	4.412E-15	4.771E-16
59848.26480	B10.7	10.62	2.128E-14	8.732E-16
59848.26879	Q1	17.75	1.230E-14	6.405E-16
59848.27302	B10.7	10.62	2.267E-14	9.314E-16
59848.27736	B10.7	10.62	2.143E-14	8.817E-16
59848.27985	J8.9	8.7	1.862E-14	6.736E-16
59848.28178	B10.7	10.62	2.233E-14	9.168E-16
59848.28428	B12.4	12.4	2.239E-14	1.018E-15
59848.28710	B10.7	10.62	2.229E-14	9.160E-16
59848.28930	J8.9	8.7	1.803E-14	6.541E-16
59848.29120	B10.7	10.62	2.101E-14	8.625E-16
59848.29299	B12.4	12.4	1.959E-14	8.874E-16
59848.29480	B10.7	10.62	2.173E-14	8.954E-16
59848.29779	B10.7	10.62	2.236E-14	9.198E-16
59848.30293	<i>M</i> - Band	4.74	4.498E-15	4.482E-16
59848.30766	B10.7	10.62	2.256E-14	9.297E-16
59848.31173	Q1	17.75	1.227E-14	6.262E-16
59848.31617	B10.7	10.62	2.146E-14	8.827E-16



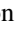

Note. Note that the observation dates are for mid-observation and include light-time corrections.





Table A3
ESO VLT VISIR Spectrum of Didymos Acquired on MJD 59848.37869
Including Light-time Correction

Wavelength (μm)	Observed Flux ($\text{W m}^{-2} \mu\text{m}^{-1}$)
8.0	1.720E-14
8.1	1.709E-14
8.2	1.722E-14
8.3	1.793E-14
8.4	1.839E-14
8.5	1.888E-14
8.6	1.922E-14
8.7	1.937E-14
8.8	1.972E-14
8.9	1.999E-14
9.0	2.001E-14
9.1	2.025E-14
9.2	2.063E-14
9.3	2.072E-14
9.4	2.044E-14
9.5	2.189E-14
9.6	2.105E-14
9.7	2.185E-14
9.8	2.176E-14
9.9	2.178E-14
10.0	2.169E-14
10.1	2.180E-14
10.2	2.177E-14
10.3	2.171E-14
10.4	2.196E-14
10.5	2.184E-14
10.6	2.162E-14
10.7	2.153E-14
10.8	2.155E-14
10.9	2.166E-14
11.0	2.166E-14
11.1	2.169E-14
11.2	2.153E-14
11.3	2.140E-14
11.4	2.120E-14
11.5	2.124E-14
11.6	2.125E-14
11.7	2.084E-14
11.8	2.098E-14
11.9	2.095E-14
12.0	2.085E-14
12.1	2.063E-14
12.2	2.043E-14
12.3	2.025E-14
12.4	1.995E-14
12.5	1.996E-14
12.6	2.003E-14
12.7	1.977E-14
12.8	1.973E-14
12.9	1.924E-14
13.0	1.934E-14

Note. Note that the flux uncertainty is estimated to be 2.2% for all wavelengths.

ORCID iDs

Benjamin Rozitis  <https://orcid.org/0000-0001-9893-241X>
 Simon F. Green  <https://orcid.org/0000-0002-9153-9786>
 Samuel L. Jackson  <https://orcid.org/0000-0001-9242-4254>
 Colin Snodgrass  <https://orcid.org/0000-0001-9328-2905>
 Cyrielle Opitom  <https://orcid.org/0000-0002-9298-7484>
 Thomas G. Müller  <https://orcid.org/0000-0002-0717-0462>
 Ulrich C. Kolb  <https://orcid.org/0000-0001-8670-8365>

Steven R. Chesley  <https://orcid.org/0000-0003-3240-6497>
 R. Terik Daly  <https://orcid.org/0000-0002-1320-2985>
 Cristina A. Thomas  <https://orcid.org/0000-0003-3091-5757>
 Andrew S. Rivkin  <https://orcid.org/0000-0002-9939-9976>

References

- Bandfield, J. L., Hayne, P. O., Williams, J.-P., et al. 2015, *Icar*, **248**, 357
 Barnouin, O., Ballouz, R.-L., Marchi, S., et al. 2023, *NatCo*, submitted
 Bertin, E., & Arnouts, S. 1996, *A&AS*, **117**, 393
 Bessell, M. S., Castelli, F., & Plez, B. 1998, *A&A*, **333**, 231
 Biele, J., Kühr, E., Senshu, H., et al. 2019, *PEPS*, **6**, 48
 Bottke, W. F., Vokrouhlický, D., Rubincam, D. P., & Nesvorný, D. 2006, *AREPS*, **34**, 157
 Bowell, E., Hapke, B., Domingue, D., et al. 1989, in *Asteroids II*, ed. R. P. Binzel, T. Gehrels, & M. S. Matthews (Tucson, AZ: Univ. Arizona Press), 524
 Bramble, M. S., Milliken, R. E., & Patterson, W. R., III 2021a, *Icar*, **369**, 114251
 Bramble, M. S., Milliken, R. E., & Patterson, W. R., III 2021b, *Icar*, **369**, 114561
 Cambioni, S., Delbo, M., Poggiali, G., et al. 2021, *Natur*, **598**, 49
 Chan, Q. H., Stephant, A., Franchi, I. A., et al. 2021, *NatSR*, **11**, 5125
 Cheng, A. F., Agrusa, H. F., Barbee, B. W., et al. 2023, *Natur*, **616**, 457
 Cheng, A. F., Rivkin, A. S., Michel, P., et al. 2018, *P&SS*, **157**, 104
 Cignoni, P., Callieri, M., Corsini, M., et al. 2008, in *Eurographics Italian Chapter Conf. 2008*, ed. V. Scarano, R. De Chiara, & U. Erra (Eurographics Assoc.)
 Cohen, M., Walker, R. G., Carter, B., et al. 1999, *AJ*, **117**, 1864
 Collins, K. A., Kielkopf, J. F., Stassun, K. G., & Hessman, F. V. 2017, *AJ*, **153**, 77
 Daly, M. G., Barnouin, O. S., Seabrook, J. A., et al. 2020, *SciA*, **6**, eabd3649
 Daly, R. T., Ernst, C. M., Barnouin, O. S., et al. 2023, *Natur*, **616**, 443
 Daly, R. T., Ernst, C. M., Barnouin, O. S., et al. 2024, *PSJ*, **5**, 24
 Davidsson, B. J. R., Rickman, H., Bandfield, J. L., et al. 2015, *Icar*, **252**, 1
 Delbo, M., dell'Oro, A., Harris, A. W., et al. 2007, *Icar*, **190**, 236
 Delbo, M., Mueller, M., Emery, J. P., Rozitis, B., & Capria, M. T. 2015, in *Asteroids IV*, ed. P. Michel, F. E. DeMeo, & W. F. Bottke (Tucson, AZ: Univ. Arizona Press) doi:10.2458/azu_uapress_9780816532131-ch006
 Delbo, M., & Tanga, P. 2009, *P&SS*, **57**, 259
 Delbo, M., Walsh, K., Mueller, M., et al. 2011, *Icar*, **212**, 138
 Domingue, D. L., Robinson, M., Carcich, B., et al. 2002, *Icar*, **155**, 205
 Farnocchia, D., Seligman, D. Z., Granvik, M., et al. 2023, *PSJ*, **4**, 29
 Fenucci, M., Novaković, B., & Marčeta, D. 2023, *A&A*, **675**, A134
 Fowler, J. W., & Chillemi, J. R. 1992, *The IRAS Minor Planet Survey Tech. Rep. PL-TR-92-2049*, Hanscom AFB, MA: Phillips Lab.
 Freuding, W., Romaniello, M., Bramich, D. M., et al. 2013, *A&A*, **559**, A96
 Garcia, R. F., Murdoch, N., & Mimoun, D. 2015, *Icar*, **253**, 159
 Gaskell, R. W., Barnouin, O. S., Scheeres, D. J., et al. 2008, *M&PS*, **43**, 1049
 Golish, D. R., Li, J.-Y., Clark, B. E., et al. 2021, *PSJ*, **2**, 124
 Graykowski, A., Lambert, R. A., Marchis, F., et al. 2017, *A&A*, **601**, A114
 Green, S. F., Eaton, N., Aitken, D. K., Roche, P. F., & Meadows, A. J. 1985, *Icar*, **62**, 282
 Grott, M., Knollenberg, J., Hamm, M., et al. 2019, *NatAs*, **3**, 971
 Gueymard, C. A. 2004, *SoEn*, **76**, 423
 Gundlach, B., & Blum, J. 2013, *Icar*, **223**, 479
 Hanuš, J., Delbo, M., Ďurech, J., & Alí-Lagoa, V. 2015, *Icar*, **256**, 101
 Hanuš, J., Delbo, M., Ďurech, J., & Alí-Lagoa, V. 2018a, *Icar*, **309**, 297
 Hanuš, J., Viikinkoski, M., Marchis, F., et al. 2017, *A&A*, **601**, A114
 Hanuš, J., Vokrouhlický, D., Delbo, M., et al. 2018b, *A&A*, **620**, L8
 Hapke, B. 2012, *Theory of Reflectance and Emittance Spectroscopy* (Cambridge: Cambridge Univ. Press)
 Harris, A. W. 1998, *Icar*, **131**, 291
 Harris, A. W., & Drube, L. 2016, *ApJ*, **832**, 127
 Helfenstein, P., & Veverka, J. 1989, in *Asteroids II*, ed. R. P. Binzel, T. Gehrels, & M. S. Matthews (Tucson, AZ: Univ. Arizona Press), 557
 Holsapple, K. A. 1993, *AREPS*, **21**, 333
 Hudson, S. 1994, *Remote Sensing Reviews*, **8**, 195
 Hung, D., Hanuš, J., Masiero, J. R., & Tholen, D. J. 2022, *PSJ*, **3**, 56
 Jackson, S. L., Kolb, U. C., & Green, S. F. 2021, *PASP*, **133**, 075003
 Jackson, S. L., Rozitis, B., Dover, L. R., et al. 2022, *MNRAS*, **513**, 3076
 Jawin, E. R., McCoy, T. J., Walsh, K. J., et al. 2022, *Icar*, **381**, 114992
 Kaasalainen, M., & Torppa, J. 2001, *Icar*, **153**, 24
 Katsalouni, K., Abe, M., Mito, H., et al. 2004, *LPSC*, **35**, 1623
 Kolb, U., Brodeur, M., Braithwaite, N., & Minocha, S. 2018, *RTSRE*, **1**, 127
 Lagage, P. O., Pel, J. W., Authier, M., et al. 2004, *Msngr*, **117**, 12
 Lagerros, J. S. V. 1998, *A&A*, **332**, 1123
 Lang, D., Hogg, D. W., Mierle, K., Blanton, M., & Roweis, S. 2010, *AJ*, **139**, 1782
 Li, J.-Y., Hirabayashi, M., Farnham, T. L., et al. 2023, *Natur*, **616**, 452
 Li, J.-Y., Zou, X.-D., Golish, D. R., et al. 2021, *PSJ*, **2**, 117
 MacLennan, E. M., & Emery, J. P. 2021, *PSJ*, **2**, 161
 MacLennan, E. M., & Emery, J. P. 2022, *PSJ*, **3**, 47
 Marchis, F., Enriquez, J. E., Emery, J. P., et al. 2012, *Icar*, **221**, 1130
 Marciniak, A., Alí-Lagoa, V., Müller, T. G., et al. 2019, *A&A*, **625**, A139
 Marciniak, A., Ďurech, J., Alí-Lagoa, V., et al. 2021, *A&A*, **654**, A87
 Maturilli, A., Helbert, J., Ferrari, S., & D'Amore, M. 2016, *EP&S*, **68**, 84
 McGraw, L. E., Emery, J. P., Thomas, C. A., et al. 2022, *PSJ*, **3**, 243
 Michel, P., Küppers, M., Bagatin, A. C., et al. 2022, *PSJ*, **3**, 160
 Mueller, M. 2012, PhD thesis, Freie Univ. Berlin
 Mueller, M., Marchis, F., Emery, J. P., et al. 2010, *Icar*, **205**, 505
 Müller, T. G., Burgdorf, M., Alí-Lagoa, V., et al. 2021, *A&A*, **650**, A38
 Müller, T. G., Hasegawa, S., & Usui, F. 2014, *PASJ*, **66**, 52
 Müller, T. G., Marciniak, A., Kiss, Cs., et al. 2018, *ASR*, **62**, 2326
 Müller, T. G., O'Rourke, L., Barucci, A. M., et al. 2012, *A&A*, **548**, A36
 Müller, T. G., Sekiguchi, T., Kaasalainen, M., et al. 2005, *A&A*, **443**, 347
 Naidu, S. P., Chesley, S. R., Moskovitz, N., et al. 2023, *PSJ*, submitted
 Okada, T., Fukuhara, T., Tanaka, S., et al. 2020, *Natur*, **579**, 518
 Okada, T., Tanaka, S., Sakatani, N., et al. 2022, *LPSC*, **53**, 1319
 Opeil, C. P., Consolmagno, G. J., & Britt, D. T. 2010, *Icar*, **208**, 449
 Oszkiewicz, D. A., Bowell, E., Wasserman, L. H., et al. 2012, *Icar*, **219**, 283
 Penttilä, A., Shevchenko, V. G., Wilkman, O., & Muinonen, K. 2016, *P&SS*, **123**, 117
 Polishook, D., DeMeo, F. E., Burt, B. J., et al. 2023, *PSJ*, **4**, 229
 Pravec, P., Harris, A. W., Kušnirák, P., et al. 2012, *Icar*, **221**, 365
 Pravec, P., Scheirich, P., Kušnirák, P., et al. 2006, *Icar*, **181**, 63
 Pravec, P., Thomas, C. A., Rivkin, A. S., et al. 2022, *PSJ*, **3**, 175
 Rivkin, A. S., Howell, E. S., Emery, J. P., & sunshine, J. 2018, *Icar*, **304**, 74
 Rivkin, A. S., Thomas, C. A., Wong, I., et al. 2023, *PSJ*, **4**, 214
 Robinson, M. S., Thomas, P. C., Veverka, J., Murchie, S. L., & Wilcox, B. B. 2002, *M&PS*, **37**, 1651
 Roth, N. X., Milam, S. N., Remijan, A. J., et al. 2023, *PSJ*, **4**, 206
 Rozitis, B. 2017, *MNRAS*, **464**, 915
 Rozitis, B., Duddy, S. R., Green, S. F., & Lowry, S. C. 2013, *A&A*, **555**, A20
 Rozitis, B., Emery, J. P., Sielger, M. A., et al. 2020a, *JGRE*, **125**, e06323
 Rozitis, B., & Green, S. F. 2011, *MNRAS*, **415**, 2042
 Rozitis, B., & Green, S. F. 2012, *MNRAS*, **423**, 367
 Rozitis, B., & Green, S. F. 2013, *MNRAS*, **433**, 603
 Rozitis, B., Green, S. F., Jackson, S. L., et al. 2023, *Asteroids, Comets, Meteors Conf.*, 2115
 Rozitis, B., Green, S. F., MacLennan, E., & Emery, J. P. 2018, *MNRAS*, **477**, 1782
 Rozitis, B., MacLennan, E., & Emery, J. P. 2014, *Natur*, **512**, 174
 Rozitis, B., Ryan, A. J., Emery, J. P., et al. 2020b, *SciA*, **6**, eabc3699
 Rozitis, B., Ryan, A. J., Emery, J. P., et al. 2022, *JGRE*, **127**, e07153
 Saito, J., Miyamoto, H., Nakamura, R., et al. 2006, *Sci*, **312**, 1341
 Sakatani, N., Ogawa, K., Iijima, Y., et al. 2017, *AIPA*, **7**, 015310
 Sakatani, N., Tanaka, S., Okada, T., et al. 2021, *NatAs*, **5**, 766
 Sánchez, P., & Scheeres, D. J. 2020, *Icar*, **338**, 113443
 Scheirich, P., & Pravec, P. 2022, *PSJ*, **3**, 163
 Schorghofer, N. 2008, *ApJ*, **682**, 697
 Schörghofer, N., Hsieh, H. H., Novaković, B., & Walsh, K. J. 2020, *Icar*, **348**, 113865
 Seligman, D. Z., Farnocchia, D., Micheli, M., et al. 2023, *PSJ*, **4**, 35
 Shepard, M. K., Campbell, B. A., Bulmer, M. H., et al. 2001, *JGR*, **106**, 32777
 Shimaki, Y., Senshu, H., Sakatani, N., et al. 2020, *Icar*, **348**, 113835
 Spencer, J. R. 1990, *Icar*, **83**, 27
 Statter, T. S. 2015, *Icar*, **248**, 313
 Thomas, C. A., Naidu, S. P., Scheirich, P., et al. 2023, *Natur*, **616**, 448
 Tonry, J. L., Stubbs, C. W., Lykke, K. R., et al. 2012, *ApJ*, **750**, 99
 Trógolo, N., Bagatin, A. C., Moreno, F., & Benavidez, P. G. 2023, *Icar*, **397**, 115521
 Vernazza, P., Carry, B., Emery, J., et al. 2010, *Icar*, **207**, 800
 Veverka, J., Thomas, P. C., Robinson, M., et al. 2001, *Sci*, **292**, 484
 Vokrouhlický, D., Bottke, W. F., Chesley, S. R., Scheeres, D. J., & Statter, T. S. 2015, in *Asteroids IV*, ed. P. Michel, F. E. DeMeo, & W. F. Bottke (Tucson, AZ: Univ. Arizona Press)
 Walsh, K. J., Richardson, D. C., & Michel, P. 2008, *Natur*, **454**, 188
 Werner, R. A., & Scheeres, D. J. 1996, *CeMDA*, **65**, 313
 Williams, G. V. 2013, PhD thesis, Open Univ., Milton Keynes, UK
 Wolters, S. D., Rozitis, B., Duddy, S. R., et al. 2011, *MNRAS*, **418**, 1246
 Yano, H., Kubota, T., Miyamoto, H., et al. 2006, *Sci*, **312**, 1350
 Yu, L., Ji, J., Wang, S., et al. 2014, *MNRAS*, **439**, 3357